Matrix Degradability Contributes to the Development of Salivary Gland Progenitor Cells with Secretory Functions

Apoorva S. Metkari,[1] Eric W. Fowler,[1*] Robert L. Witt,[2] and Xinqiao Jia[1,3,4,5*]

[1]Department of Materials Science and Engineering, University of Delaware, Newark, Delaware, USA

[2]Helen F. Graham Cancer Center and Research Institute, Newark, Delaware, USA

[3]Department of Biomedical Engineering, University of Delaware, Newark, Delaware, USA

[4]Department of Biological Sciences, University of Delaware, Newark, Delaware, USA

[5]Delaware Biotechnology Institute, 590 Avenue 1743, Newark, Delaware, USA

*To whom correspondence should be addressed:

Eric W. Fowler, Ph.D., Department of Materials Science and Engineering, University of Delaware, Newark, DE, 19716, USA. Email: fowlere@udel.edu

Xinqiao Jia, Ph.D., Department of Materials Science and Engineering, University of Delaware, Newark, DE, 19716, USA. E-mail: xjia@udel.edu

Keywords: Salivary gland, stem/progenitor cells, matrix degradation, MMP, c-KIT.

ABSTRACT

Synthetic matrices that are cytocompatible, cell adhesive and cell responsive are needed for the engineering of implantable, secretory salivary gland constructs to treat radiation induced xerostomia or dry mouth. Here, taking advantage of the bioorthogonality of the Michael-type addition reaction, hydrogels with comparable stiffness but varying degrees of degradability (100% degradable: 100DEG; 50% degradable: 50DEG; and non-degradable: 0DEG) by cell-secreted matrix metalloproteases (MMPs) were synthesized using thiolated HA (HA-SH), maleimide (MI)-conjugated integrin-binding peptide (RGD-MI) and MI-functionalized peptide crosslinkers that are protease degradable (GIW-bisMI) or non-degradable (GIQ-bisMI). Organized multicellular structures developed readily in all hydrogels from dispersed primary human salivary gland stem/progenitor cells (hS/PCs). As the matrix became progressively degradable, cells proliferated more readily and the multicellular structures became larger, less spherical, and more lobular. Immunocytochemical analysis showed positive staining for stem/progenitor cell markers CD44 and keratin 5 (K5) in all three types of cultures, and positive staining for the acinar marker α-amylase under 50DEG and 100DEG conditions. Quantitatively at the mRNA level, the expression levels of key stem/progenitor markers *KIT*, *KRT5,* and *ETV4/5* were significantly increased in the degradable gels as compared to the non-degradable counterparts. Western blot analyses revealed that imparting matrix degradation led to >3.8-fold increase in KIT expression by day 15. The MMP-degradable hydrogels also promoted the development of a secretary phenotype, as evidenced by the upregulation of acinar markers α-amylase (*AMY*), aquaporin-5 (*AQP5*), and sodium-potassium-chloride cotransporter 1 (*SLC12A2*). Collectively, we show that cell-mediated matrix remodeling is necessary for the development of regenerative pro-acinar progenitor cells from hS/PCs.

INTRODUCTION

Head and neck cancers account for nearly 1.1 million cases worldwide and is the seventh most common cancer type.[1] In the United States, 54,000 head and neck cases are detected every year with more than 11,000 deaths per year.[2] Radiation therapy is frequently used in the management of head and neck malignancies, either as a stand-alone therapy or in combination with surgery and chemotherapy.[3] Such treatment improves the disease outcome, but is associated with significant treatment-related side effects. Particularly, an estimated 50-80% of head and neck cancer patients experience radiation-induced salivary gland hypofunction, i.e. xerostomia or dry month.[4] Damage to the salivary gland tissue can occur with doses as low as 26 Gy, which is less than half the dose typically used to treat head and neck cancers.[5] Radiation-induced xerostomia is characterized by irreversible damage to the saliva-producing acinar cells.[6] In salivary glands exposed to radiation, dilated vasculature, altered neuronal innervation, and fibrosis are also observed.[7-8] Moreover, the innate regeneration capabilities are impaired owing to the significant depletion of tissue-resident stem/progenitor cells.[9] As a result of reduced salivary flow, patients not only have higher rates of dental caries, periodontal diseases, and oral infections, but also experience reduced general health, nutrition, and quality of life.[10] Therapeutic relief can be achieved by implantation of an engineered gland derived from autologous salivary gland stem/progenitor cells isolated prior to radiation treatment and grown in a customized synthetic matrix.

The extracellular matrix (ECM) regulates the growth, differentiation, and homeostasis of the resident cells.[11] When epithelial cells isolated from branched glandular tissues are expanded in two-dimensional (2D) cultures, they lose their stemness and exhibit altered gene expression patterns.[12-13] To mimic key aspects of tissue composition, architecture, and mechanics, synthetic matrices with responsive and instructive cues have been used to reconstitute the epithelial tissues *in vitro*. Salivary gland epithelial cells isolated from human and rodent tissues have been cultured in hydrogels based on polyethylene glycol (PEG),[14, 15] collagen,[16] alginate,[17] fibrin,[18] and hyaluronic acid (HA).[19, 20] As a ubiquitous non-sulphated glycosaminoglycan in natural ECM, HA not only modulates tissue viscoelasticity but also binds

with cell surface receptors CD44 and RHAMM to activate various cell signalling pathways.[21] Using blank HA gels, we identified the optimal matrix stiffness for the development of acini-like multicellular spheroids from dispersed primary human salivary gland stem/progenitor cells (hS/PCs).[22] Incorporation of peptides derived from fibronectin (RGDSP) and perlecan domain IV (TWSKV) further accelerated the development of multicellular spheroids expressing key progenitor markers keratin 5 (K5) and keratin 14 (K14) and the acinar marker α-amylase (AMY).[19] Notably, supplementation of RGD cultures with a pharmacological inhibitor of transforming growth factor-β (TGF-β) receptor repressed cellular expression of keratin 7 (K7), a ductal marker and frequently associated with cellular stress, while maintaining rapid expansion of α-amylase-expressing spheroids.[19]

From the tissue regeneration perspective, it is important to maintain a pool of stem/progenitor cells to ensure self-maintenance and continuous renewal of differentiated cells during *in vitro* culture and after implantation.[23-26] In addition to K5/K14, KIT, a receptor tyrosine kinase encoded by the oncogene c-KIT, has been shown to mark progenitors in developing organs.[23] Although K14+ cells activate a multipotency program to give rise to both acinar and ductal cell lineages, the main source of replacement acinar cells after tissue damage is KIT+ progenitor cells.[26] In fact, KIT is expressed by a subset of K14+ progenitors, and KIT deficient embryonic day 14 (E14) mouse exhibits reduced epithelial branching. Moreover, KIT and FGFR2b signalling are important for the expansion and maintenance of the distal progenitors;[27] transplantation of KIT+ cells led to the restoration of glandular function in mice.[24] Unfortunately, our cell isolation and culture protocols gave rise to hS/PCs with significantly reduced KIT expression as compared to the parotid gland.[20]

In addition to matrix stiffness and ligand density, matrix degradability has been shown to have profound effects on stem cell functions.[28, 29] Cell-mediated matrix remodeling through secreted matrix metalloproteases (MMPs) has been shown to preserve the stemness of neural progenitor cells[28] and promote the chondrogenesis or osteogenesis of mesenchymal stem cells.[30] Importantly, degradation-mediated cellular traction directs stem cell fate in covalently crosslinked 3D gels.[31] Finally, MMP-mediated matrix degradation is necessary for mouse

primary submandibular gland cells to maintain their stemness and to differentiate into acinar cells.[14]

We hypothesize that promoting bi-directional cell-matrix interactions by imparting MMP-degradability in our custom RGD-decorated HA gels will lead to the development of secretory constructs with regenerative capacities. Here, cell-adhesive HA hydrogels with variable degradability were prepared using peptide-based crosslinkers that are susceptible or resistant to degradation by MMPs. We examine how cell-mediated matrix degradation influences the proliferation, organization, and phenotype of encapsulated hS/PCs employing qPCR, immunocytochemistry, and western blotting techniques. We further quantify the expression and production of MMPs and TIMPs during culture at different time points. The degradable hydrogels stimulate the expansion and growth of pro-acinar stem/progenitor cells, with a ~50-fold enhancement in *KIT* expression at the transcript level. Overall, imparting MMP-degradable crosslinks in covalently crosslinked HA gels enhanced the regenerative potential of hS/PCs.

EXPERIMENTAL SECTION

Synthesis of Hydrogel Precursors

Thiolated HA (HA-SH), with a 60% thiol incorporation as determined by ^{1}H NMR (Figure S1), was synthesized following our reported protocols.[19, 32] Cell adhesive peptide (RGD, GGGRGDSPG), and MMP-degradable (GIW, GKRDGPQG↓IWGQDRKG) and non-degradable (GIQ, GKRDGIQQWGGPDRKG) peptides were prepared using a CEM liberty blue peptide synthesizer (CEM Corporation, Mathews, NC) employing standard Fmoc-based solid phase synthesis protocol on Rink Amide AM resin (AAPPTec, Louisville, KY) at a 0.25 mmol scale. Maleimide was conjugated to RGD on resin through the N-terminal amine via the reaction with 4-maleimidobutyric acid, as previously described.[19] Separately, maleimide was introduced to GIW/GIQ on resin via the lysine amines. For selective protection of the lysine amine, Nα-Fmoc-Nε-(4-methyltrityl) L-lysine was used. After acetylation of the N-terminal amine with acetic anhydride in dimethylformamide (DMF) with *N*,*N*-diisopropylethylamine

(DIPEA), lysine amines were selectively deprotected with 3% (v/v) trifluoroacetic acid (TFA) in dichloromethane (DCM). The resin was subsequently mixed with 4-maleimidobutyric acid (8×) for 2 h with O-benzotriazole-N,N,N′,N′-tetramethyluronium hexafluorophosphate (HBTU, 8×) and DIPEA (8×) in DMF. Peptides were cleaved from the resin by a 3 h treatment with TFA/triisopropylsilane (TIPS)/H_2O (95:2.5:2.5, v/v) cocktail. The crude product was precipitated in cold diethyl ether. Purification was carried out using reverse-phase high-performance liquid chromatography (RP-HPLC) with a mobile phase of acetonitrile/water with 0.1% TFA. Peptide purity and mass (Figure S2-S7) were verified using a Waters UPLC LC-MS/MS system equipped with an ESI source (Xevo G2-S QTof) and a Shimadzu HPLC (Shimadzu Corporation, Kyoto, Japan), respectively. Products were stored as a lyophilized powder at −20 °C.

Hydrogel Preparation

HA-SH was dissolved in DI water at 2 wt% and the pH was adjusted to 6.4 using citrate phosphate buffer. Stock solutions of RGD-MI and GIW-bisMI and/or GIQ-bisMI buffered at pH 6.4 were added to HA-SH at 4°C (thiol/MI molar ratio of 1:1) to establish crosslinked gel disks. Gelation time was determined by monitoring the viscosity of the reaction mixture over time[33] using a TA Instruments (New Castle, DE) AR-G2 rheometer (Figure S8). Hydrogels with variable degradability (Table 1) were made by adjusting the molar ratio of GIW-bisMI / GIQ-bisMI while maintaining the concentrations of HA-SH, bisMI crosslinkers, and RGD-MI constant.

Table 1: Formulations of HA hydrogels with varying susceptibility to MMP-mediated degradation.

Gel component	Non-degradable (0DEG)	50% degradable (50DEG)	100% degradable (100DEG)
HA-SH	0.65 wt%	0.65 wt%	0.65 wt%
RGD-MI	3 mM	3 mM	3 mM
GIW-bisMI	0 mM	1.5 mM	3 mM
GIQ-bisMI	3 mM	1.5 mM	0 mM

Hydrogel Characterization

Hydrogel stiffness was determined using a TA Instruments DHR-3 rheometer with a 20-mm cone-and-plate geometry at 25°C. Promptly after mixing on ice, the precursor mixture was loaded on the plate, and mineral oil was applied around the geometry to prevent evaporation. A time sweep was performed with 0.1% strain at 1 Hz and a frequency sweep (Figure S9) from 0.1 to 10 Hz was performed at 0.1% strain. Measurements were conducted in triplicate, and the average storage (G′) and loss (G″) moduli are reported. Fully crosslinked hydrogel disks were incubated in PBS for 30 min, which was then replaced with 100 U/mL of collagenase IV in a 5 mM calcium chloride solution. Every 30 min, the hydrogel mass was recorded, and the collagenase IV solution was refreshed. Hydrogel degradation was monitored gravimetrically until the 100DEG sample was completely degraded. The mass of the remaining gel was normalized to that of the swollen gel. Measurements were conducted with three repeats for each time point.

3D Culture of hS/PCs

Following our reported procedures,[19, 34, 35] hS/PCs were isolated from normal human parotid tissues obtained from consenting patients undergoing parotidectomy with approved protocols by Christiana Care and the University of Delaware. The tissue was first washed with F-12 media (Invitrogen, Carlsbad, CA) containing 1% (v/v) Betadine solution. Next, blood vessels and connecting tissues were removed, and the remaining tissue was finely minced in 1 mL HepatoSTIM media (Corning Inc., Corning, NY) to a slurry. After diluting with additional media to a final volume of 12 mL, the slurry was aliquoted to a 6-well plate at 2 mL per well. hS/PCs were maintained in HepatoSTIM medium supplemented with penicillin-streptomycin (100 U/mL), amphotericin B (1%, v/v), and epidermal growth factor (EGF, 10 ng/mL, Corning Inc.). At 70-80% confluence, cells were treated with trypsin-EDTA (0.05%, w/v) for 3 min. After the residual trypsin was neutralized with a trypsin soybean inhibitor (Sigma Aldrich, Burlington, MA), cells were passaged for subculture. Experiments were conducted with cells isolated from a 25-year-old female donor at passages between 3-6. Additional experiments were conducted with cells isolated from a 70-year-old male. To establish 3D cell-laden gel constructs, hS/PCs

were suspended in HBSS and reconstituted in 2 wt% sterile HA-SH before bisMI crosslinkers and the RGD-MI solutions were added. The final hS/PC concentration in all constructs was 3×10^6 cells/mL. The HepatoSTIM media was added 5 min after the gel was formed. Media was refreshed every two days.

Cell Morphology

Cellular constructs were inspected regularly with Nikon Eclipse Ti series microscope in brightfield view. Separately, constructs were fixed with 4% paraformaldehyde (PFA, Sigma Aldrich) in PBS for 1 h at room temperature, washed with PBS three times (10 min each), permeabilized with 0.1% Triton for 30 min and blocked with 3% (w/v) bovine serum albumin (BSA) overnight at room temperature. Samples were then incubated with Alexa Fluor 568 Phalloidin (1:400 dilution, Life Technologies, Carlsbad, CA) for 16 h at room temperature, followed by three PBS washes (10 min each). Next, samples were incubated with Hoechst 33342 (1:1000 dilution, Life Technologies) for 30 min at room temperature. Three PBS washes were performed (10 min each). Confocal imaging was performed using a Zeiss LSM 880 equipped with an Airyscan detector in Fast Airyscan mode. Images were captured as z-stacks of 101.18 µm and maximum intensity projection was performed (Figure S10). Feret's diameter and circularity were quantified with ImageJ software.

Cell Viability and Proliferation

Cell viability was analyzed by LIVE/DEAD assay (Thermo Fisher Scientific, Waltham, MA). Calcein AM (1:1000), ethidium homodimer 1 (EthD-1, 1:2000), and Hoechst 33342 (1:1000) were diluted in PBS and incubated with cell-laden gels for 30 min at 37°C. Confocal images were captured on Zeiss LSM 880 microscope equipped with an Airyscan detector using a 10xC-Apochromat 0.45 NA water immersion objective. Z-stack images of 101.18 µm were obtained and maximum intensity projection was performed (Figure S11). Cell viability was calculated using ImageJ software by counting cells stained by Hoechst (total cells, Figure S12) and EthD-1 (dead cells). Cell proliferation was determined as the fold change in the

number of viable cells on a given day relative to that for day 1. Spheroids were defined as structures with three or more cells labelled with Hoechst and calcein. Spheroid forming efficiency is defined as the number of spheroids found on a given day divided by the total number of cells present on day 1.

RNA Extraction

Cellular constructs were snap-frozen on an isopropanol/dry ice mixture and crushed with a pestle. The gel slurry was allowed to dissociate in 1 mL Trizol solution (Invitrogen, Carlsbad, CA). After mixing with 200 µL chloroform, the solution was centrifuged at 12,000 ×g at 4°C for 15 min and the aqueous layer was collected. An equal amount of 100% ethanol was subsequently added, and the aqueous solution was transferred to an RNA extraction column (Zymo Research, Irvine, CA) and centrifuged at 16,000 ×g for 30 s at room temperature. Next, 400 µL of RNA prep buffer (Zymo Research) was added and the column was centrifuged at 16,000 ×g for 30 s. The column was then repeatedly (3 times) cleaned with the wash solution (Zymo Research) and centrifuged. Finally, 12 µL nuclease free DEPC-treated water was added and the column was centrifuged at 16,000 ×g for 2 min. The aqueous eluents were pooled, and RNA quantification and purity were assessed using a NanoDrop 2000 Spectrophotometer (Nanodrop Technologies, Wilmington, DE). This technique yielded high-purity RNA with absorbance ratios at λ of 260/280 nm >2.01 and 260/230 >1.95.

Quantitative Polymerase Chain Reaction (qPCR)

RNA was reverse transcribed using the QuantiTect Reverse Transcription Kit (QIAGEN, Hilden, Germany) following the manufacturer's protocol. Sequence-specific amplification and detection were performed on an Applied Biosystems 7300 real-time PCR machine, with a thermal cycling profile of 1 cycle at 95 °C for 10 min, followed by 40 cycles of 95 °C for 15 s and 60 °C for 1 min. PCR reactions were prepared in 96 well formats at 20 µL by combining Power SYBR™ green PCR master mix (Applied Biosystems), cDNA, and target-specific primers. Primers were synthesized by Integrated DNA Technologies (Coralville, IA),

and the complete primer sequences are available in Table S1. Glyceraldehyde 3-phosphate dehydrogenase *(GAPDH)* was used as the reference gene. Cycle threshold values were generated using 7300 System SDS RQ Study software version 1.4 (Applied Biosystems). The obtained C_T values were normalized to *GAPDH,* and the fold changes were calculated using the $\Delta\Delta C_T$ method. Three biological replicates are reported from three technical replicates measured in duplicate.

Immunofluorescence

The cell-laden hydrogels were fixed with 4% PFA for 1 h, then blocked with 3% (w/v) BSA with desired permeabilizing agents for 16 h at room temperature. Permeabilization was carried out with 0.2% Triton for K5 and α-Amylase and with 0.05% saponin for c-KIT, CD44, and β-catenin. Constructs were incubated in primary antibody solutions prepared according to Table S2 for 24 h at room temperature, washed with PBS twice (5 min each), and incubated in PBS for an additional 16 h. Samples were subsequently treated with secondary antibodies at 1:200 dilution with 3% BSA and the respective permeabilizing agents for 48 h at room temperature. Constructs were washed thrice with PBS (15 min each). Fluorescent microscopy was performed using a Zeiss LSM 880 equipped with an Airyscan detector in Fast Airyscan mode. Images were captured as a single slice.

Enzyme-Linked Immunosorbent Assay (ELISA) and Enzcheck™ Assay

Secretion of MMP1 and MMP2 was assessed using Human Total MMP1 DuoSet ELISA and Human Total MMP2 DuoSet ELISA (R&D Systems, Minneapolis, MN), respectively. Secretion of α-amylase was quantified using Human Salivary Amylase Alpha ELISA Kit (Novus Biologicals, Littleton, CO). Enzcheck gelatinase/collagenase assay (Thermo Fisher Scientific) and EnzChek Ultra Amylase Assay (Thermo Fisher Scientific) were also performed on the media collected from day 1 and day 15. All assays were performed following the manufacturer's protocols, and measurements were made using a SpectraMax i3x Multi-

Mode Microplate Reader (Molecular Devices, San Jose, CA). Protein levels were normalized to the number of cells at each time point based on Hoechst staining.

Protein Extraction

To prepare the extraction buffer, 1/10 volume of 30× dithiothreitol (DTT) reducing buffer (Cell Signaling Technology, Danvers, MA) was added to 1 volume of 3× sodium dodecyl sulfate (SDS) loading buffer (Cell Signaling Technology, Danvers, MA). This buffer was diluted three times with DI water to obtain the final 1× SDS buffer. In a 1.5 mL Eppendorf tube with 500 µL 1× SDS buffer, the construct was crushed and sonicated three times (1 min each). The mixture was centrifuged at 400 ×g for 5 min and the supernatant was collected as the cell lysate. The protein concentration was quantified using a Micro BCA™ Protein Assay Kit (Thermo Fisher Scientific) following the manufacturer's protocol, and the measurements were obtained using SpectraMax® i3x Multi-Mode Microplate Reader.

Western Blotting

The cell lysate was diluted to the required protein amount using the cell lysis buffer (1× SDS loading buffer and 1× DTT reducing buffer). The solution was heated at 95 °C for 10 min and vortexed for 30 s before centrifuging at 15,000 ×g for 2 min at room temperature. SDS-polyacrylamide gel electrophoresis (SDS-PAGE) was carried out using 4–20% Mini-PROTEAN TGX Stain-Free Protein Gels (Bio-Rad Laboratories, Hercules, CA) incubated with Tris-Glycine-SDS buffer (Bio-Rad Laboratories). Sample lysate was loaded at 30 µg per lane and a 40-volt current was applied for 30 min, followed by 200 volts for 40 min at 4 °C. Samples were transferred to nitrocellulose membranes (Cell Signaling Technology, Danvers, MA) at 4 °C for 2 h at 70 volts. For protein lane normalization, the nitrocellulose membranes were treated with Revert 700 Total Protein Stain (LI-COR Biosciences, Lincoln, NE) according to the manufacturer's protocol and imaged using an iBright FL1500 Imaging System (Invitrogen). Membranes were blocked with 5% (w/v) skim milk in tris-buffered saline containing 0.1% Tween 20 (Cell Signalling Technology) for 1 h at room temperature. Membranes were

incubated for 24 h at 4 °C with the c-KIT primary antibody (Cell Signaling Technology) diluted at 1:1000 in 5% BSA in TBST. Membranes were next washed three times with 1× TBST at room temperature and incubated with HRP-linked secondary antibody (Cell Signalling Technology) diluted at 1:2000 in 5% skim milk in TBST for 1 h at room temperature before being washed with TBST three times at room temperature. The membranes were then treated with ECL substrate (R&D Systems) and the chemiluminescence was visualized using an iBright FL1500 Imaging System. The density of each band was quantified with ImageJ. Total protein was used as the internal control to normalize each protein lane since the expression level of housekeeping proteins can vary depending on samples and the experimental conditions.[36] Total protein was stained using Revert 700 total protein stain. The c-KIT band was normalized to the total protein stain in every condition.

Statistical Analysis

Significance was analysed by performing one-way ANOVA with a p value less than 0.05. Comparisons between pairs were made using Tukey's HSD post hoc. Statistical analysis was conducted using JMP Pro 15 (SAS Institute Inc.). Error bars represent the standard error of the mean.

RESULTS

Thiol-Maleimide Click Reaction Yields Hydrogels with Variable Degradability.

The synthetic matrices were fabricated using modular building blocks derived from HA and synthetic peptides employing an efficient thiol-maleimide ‘click’ reaction (Figure 1A). The crosslinking reaction was pH and temperature-dependent (Figure S8); gelation was instantaneous at pH 7 at ambient temperature, and gels formed under this condition were heterogeneous.[37] To ensure reproducible synthesis of the hydrogel networks and homogeneous distribution of hS/PCs in 3D, hydrogels were prepared at pH 6.4 at 4°C. The same chemistry was used to immobilize cell adhesive RGD peptide to the network as dangling side chains with maximized integrin binding capacity. HPLC analysis of the PBS solution in

contact with the synthesized hydrogel for 24 h did not show any detectable unconjugated free RGD peptide.[19]

To prepare hydrogels with different degradability, GIW-bisMI and GIQ-bisMI were introduced at a molar ratio of 0:1 (non-degradable, 0DEG), 1:1 (50% degradable, 50DEG) and 1:0 (100% degradable, 100DEG). In all formulations, the concentration of RGD and (GIW+GIQ) was maintained constant at 3 mM. Examination via oscillatory rheometry revealed that these gels exhibited comparable mechanical properties (Figure 1B), with 0DEG, 50DEG, and 100DEG having average storage (G') / loss (G") moduli of 202 ± 21 Pa / 0.35 ± 0.03 Pa, 170 ± 35 Pa / 0.19 ± 0.04 Pa, and 175 ± 28 Pa / 0.25 ± 0.08 Pa, respectively. No statistical significance was detected in gel stiffness across the three types of gels. Representative frequency sweep results are shown in Figure S9. The hydrogels swelled rapidly in PBS buffer, reaching an equilibrium swelling ratio of 49.7 ± 3.2.

Hydrogels were immersed in PBS with 100 U/mL collagenase type IV and the gel mass was measured gravimetrically every 30 min (Figure 1C). No significant decrease in gel mass was detected for 0DEG over the course of 270 min, while no gel mass remained for 100DEG after 270 min. Hydrogel degradability was found to directly correlate with the relative amount of GIW-bisMI crosslinker used; the more GIW-bisMI used, the faster the gel degraded. Taken together, the bioorthogonal approach enabled the development of hydrogels with consistent mechanical properties and RGD ligand density, but variable susceptibility to protease cleavage.

Matrix Degradation Mediates the 3D Growth and Assembly of hS/PCs.

hS/PCs were encapsulated in HA-based hydrogels of varying degradability and cultured for 15 days in HepatoStim media. At day 1, hS/PCs remained as rounded single cells homogeneously distributed throughout the network (Figure 2B). Some multicellular structures were developed as early as day 3 (Figure 2C), and by day 7, spheroids were abundant in all three types of matrices, irrespective of gel degradability. Thereafter, spheroids continued to increase in size until day 15, when the experiments were terminated. The Feret's diameter of

the spheroids increased with the culture time in all three types of gels (Figure 2C), although structures grown in 100DEG gels were significantly larger than those found in 50DEG and 0DEG gels on day 6, day 9, day 12, and day 15 ($p < 0.05$ and 0.001). By day 15, the average Feret's diameter for the multicellular assemblies established in 0DEG, 50DEG, and 100DEG was 55.8 ± 1.5 μm, 86.5 ± 3.5 μm, and 96.9 ± 3.8 μm, respectively. Day 15 spheroids found in 0DEG gels were morphologically and dimensionally similar to those grown in non-degradable HA hydrogels prepared with HA-SH, RGD-MI, and acrylated HA.[19]

Examination of the 3D cultures by confocal microscope revealed that structures developed in 0DEG gels were more compact than those found in 50DEG and 100DEG gels (Figure 2B). Quantitative assessment based on circularity confirmed the above observations (Figure 2D). With an increase in the matrix degradability, spheroid circularity progressively decreased. Spheroid circularity did not significantly deviate from 1.0 in 0DEG constructs over 15 days of culture. On the other hand, spheroid circularity decreased significantly from 0.9 ± 0.01 on day 3 to 0.43 ± 0.08 on day 15 in 100DEG cultures. By day 15, spheroids circularity across the three types of gel constructs was significantly different ($p < 0.05$ and 0.0001), with 0, 50, and 100DEG gels having spheroids with an average circularity of 0.95 ± 0.01, 0.71 ± 0.03, and 0.43 ± 0.08, respectively.

hS/PC cultures were further inspected for viability and proliferation (Figure 3). Cell viability remained high (> 87% viable) throughout the culture period across different gel formulations (Figure 3A, B). hS/PCs proliferated more in 50DEG and 100DEG gels than in the non-degradable counterpart (Figure 3C). By day 15, cells proliferated by 1.9 ± 0.3, 2.2 ± 0.5, and 2.4 ± 0.5 folds in 0DEG, 50DEG, and 100DEG gels, respectively. There was significantly more cell proliferation ($p < 0.05$) in 50DEG and 100DEG gels as compared to the 0DEG counterparts on day 15. When encapsulated in synthetic matrices as dispersed single cells, the survival and function of epithelial cells are critically dependent on the establishment of close cell-cell contacts. Spheroid-forming efficiency (SFE), defined as the number of spheroids normalized to the number of cells in the matrix on day 1, was used to quantify the effectiveness of the hydrogels in promoting clonal expansion and self-assembly of hS/PCs. While

multicellular spheroids were observed in all the hydrogels, the SFE values differed significantly depending on the matrix composition (Figure 3D). SFE for 0DEG gels increased from 36.0 ± 5.5% on day 7 to 50.0 ± 5.8% on day 15. Under 50DEG conditions, SFE increased from 41.0 ± 3.0% on day 7 to 59.0 ± 4.2% on day 15, and for 100DEG constructs, SFE increased from 48.8 ± 5.4% on day 7 to 64.5 ± 3.2% on day 15. Overall, SFE increased with culture time and matrix degradation.

Cell adhesion molecules regulate the growth and differentiation of epithelial cells and play a key role in maintaining their structural integrity.[38, 39] The predominant way in which cell-cell adhesion is realized is through the cadherin/catenin adhesion complexes. Here, we characterized the cell-cell interactions by immunofluorescence targeting β-catenin (Figure 4), which localizes to epithelial adherens junctions.[40] In 0DEG cultures, β-catenin expression was presented predominantly at the border of the spheroids interfacing with the surrounding ECM; staining between neighboring cells within the spheroid was weak. β-catenin expression in MMP-degradation matrices was distinct and strong. In 50DEG cultures, both the spheroid border and the cell-cell junctions were positively stained. β-catenin presentation in 100DEG cultures was highly localized to the apical and lateral membranes of neighboring cells. Collectively, MMP-degradable hydrogels promote the development of multicellular assemblies with β-catenin presented homogeneously in an anatomically correct fashion.[41, 42]

Degradable Matrix Promotes Cellular Secretion of Proteases

MMPs play a vital role in the remodeling of the native ECM,[43] contributing to the development of functional tissues, the maintenance of tissue homeostasis, and the establishment of pathological conditions.[44] Because the peptide crosslink (GIW) used here is the substrate for multiple MMPs,[45] we queried whether MMP expression, secretion, and activation are dependent on the degradability of the extracellular microenvironment. At the transcript level by day 15 (Figure 5A), *MMP1* expression did not vary significantly among 0DEG, 50DEG, and 100DEG conditions. 50DEG cultures promoted a significant (2.8 ± 0.1 folds, $p < 0.05$) increase in the expression of *MMP2* as compared to 0DEG cultures. *MMP2*

expression was increased significantly by 2.05 ± 0.03 folds in 100DEG cultures relative to the 0DEG counterparts ($p < 0.05$). A similar trend was observed for *MMP14* (i.e. MT1-MMP). On the other hand, cellular expression of tissue inhibitors of metalloproteinases, TIMP1 and 2, was not strongly affected by matrix composition, although TIMP3 expression was significantly higher in 100DEG (1.96 ± 0.2 folds, $p < 0.05$) and 50DEG (1.70 ± 0.06 folds, $p < 0.05$) than the non-degradable controls.

To quantify active collagenase secreted by hS/PCs maintained in various hydrogels, Enzchek assay was performed on media collected on day 1 and day 15 (Figure 5B). While the secretion level on day 1 was low under all three culture conditions, the amount of collagenase detected in day 15 cultures varied significantly; as the matrix became progressively more degradable, collagenase secretion increased accordingly. ELISA was conducted to quantify the temporal release of MMPs into the cell culture media. While MMP9 and MMP14 were not detectable, on a per cell basis, hS/PCs secreted a higher amount of MMP1 (up to 4 pg/cell) than MMP2 (up to 0.1 pg/cell). MMP1 secretion was low on day 0 but reached a steady level after day 3. MMP1 secretion was significantly greater in 100DEG cultures as compared to 50DEG and 0DEG on days 6, 9, 12, and 15 (Figure 5C). Additionally, 50DEG cultures had significantly more MMP1 secretion than 0DEG controls on days 0, 3, 6, 9, 12, and 15. Similarly, MMP2 secretion was low on day 0, increased steadily from days 3-6, and then decreased moderately from days 9-15 (Figure 5D). MMP2 secretion was not strongly dependent on matrix composition throughout the 15-day culture period, although cells in 100DEG and 50DEG gels secreted significantly ($p < 0.05$) higher amounts of MMP2 on day 3 as compared to 0DEG controls. Collectively, MMP-degradable hydrogels enhance matrix remodeling by stimulating cellular expression and secretion of matrix-degrading enzymes.

Degradable Matrix Stimulates the Expression of Stem Markers

Successful engineering of a functional salivary gland requires tissue-specific stem/progenitor cells with self-renewal capabilities. At the mRNA level by qPCR (Figure 6A), *KRT5* expression in 50DEG cultures increased 2.05 ± 0.12 folds by day 15 as compared to

the control 0DEG cultures. Further increase in matrix degradability from 50% to 100%, however, led to a significant decrease in *KRT5* expression, to a level that is slightly higher than 0DEG but is not statistically significant. There is no significant change in the gene expressions of *KRT14*, *CD44*, and *MYC* across different matrix compositions. Levels of the transcripts encoding *ETV4* and *ETV5*, transcription factors required for progenitor cell maintenance, varied significantly across different culture conditions. Increasing gel degradability increased *ETV4* expression. Compared to 0DEG cultures, the 100DEG condition induced a significant increase in *ETV4* expression (1.98 ± 0.33 folds, $p < 0.01$) and the 50DEG condition showed a significant increase of 1.75 ± 0.28 folds ($p < 0.05$). On the other hand, *ETV5* expression was significantly upregulated under 100DEG conditions as compared to 0DEG and 50DEG. Immunocytochemical analysis showed positive staining for CD44 and K5 across different culture conditions (Figure 6B, C). CD44 signals were localized on the cell surface between neighbouring cells in all three types of cultures. On the other hand, K5 signals were more localized in the cytoplasm. In 100DEG cultures, K5 signals were diffuse, with some strong patchy staining in the outer layer of cells.

Characterization of KIT expression was conducted at the mRNA level by qPCR (Figure 7A) and at the protein level by immunofluorescence (Figure 7B) and western blot (Figure 7C, Figure S14). At the transcript level, the introduction of MMP-degradable crosslinks led to a significant ($p < 0.005$, Figure 7A) upregulation of *KIT* expression. Compared to 0DEG cultures, *KIT* expression increased by 50.9 ± 1.6 and 48.2 ± 1.7 folds for 50DEG and 10DEG, respectively. A similar trend was observed using cells isolated from a 70-year-old male (Figure S15). Spheroids grown in 0DEG gels were stained positive for KIT; however, those found in 50DEG and 100DEG were staining more intensely. Results from western blotting (Figure 7C) depict a higher KIT expression in the degradable gels as compared to 0DEG gels, in agreement with the qPCR observation. Quantification of the band intensity via densitometry revealed that, compared to the control 0DEG cultures, 50DEG and 100DEG gels promoted a 4.5 ± 0.8 and 3.8 ± 0.7-fold increase in KIT expression.

Degradable Matrices Enhanced the Expression of Acinar Markers

We quantitatively analyzed transcripts encoding markers of differentiated cell phenotypes (Figure 8A). The highest expression of acinar markers *AMY*, *AQP5*, *AQP3*, and *SLC12A2* was found in 50DEG cultures. Compared to the 0DEG controls, 50DEG cultures significantly increased the expression of *AMY* ($p < 0.01$), *AQP5* ($p < 0.05$), and *SLC12A2* ($p < 0.05$) by 2.9 ± 0.3, 1.5 ± 0.4, and 1.6 ± 0.1 folds, respectively. Further increase in matrix degradability from 50DEG to 100DEG resulted in a decrease in the expression of these genes, although the transcript level for *AMY* in 100DEG cultures was still significantly higher (1.9 ± 0.4, $p < 0.01$) than that in the 0DEG counterpart. The expression of *AQP5* in 100DEG dropped below the level for 0DEG, although the difference was not statistically significant. The expression of *SLC12A2* followed a similar trend. The expression of *AQP3* was not strongly dependent on matrix degradability. The expression of ductal marker *MUC1* did not change significantly across different matrix compositions. The increase in *KRT7* expression in 50DEG was not significant as compared to the 0DEG counterparts. There was a significant decrease in the *KRT7* gene expression in 100DEG condition when compared to 0DEG and 50DEG conditions.

α-Amylase expression was further characterized at the protein level by ELISA (Figure 8B) and immunocytochemistry (Figure 8C). As the culture time extended, cells secreted more α-amylase for all three culture conditions. For all time points examined, degradable matrices (50DEG and 100DEG) stimulated the production of amylase at a significantly higher level ($p<0.05$ and $p<0.01$) than the non-degradable counterparts. Analysis of media aliquots for amylase activity via EnzCheck assay showed a similar trend (Figure S16). On day 1, active amylase content in the media was similarly low for all three types of culture conditions. By day 15, active amylase content in 50DEG and 100DEG cultures was comparable and significantly higher ($p < 0.05$) than the 0DEG controls. α-Amylase was not detectable by immunofluorescence (Figure 8C) in 0DEG cultures. By contrast, amylase was abundant throughout the spheroid developed in 50DEG and 100DEG gels. Collectively, MMP-degradable hydrogels promote the development of pro-acinar cells.

DISCUSSION

Radiotherapy results in relatively high survival rates for patients with head and neck cancers. However, an inevitable side effect of such a treatment is hyposalivation, i.e. severe reduction in saliva production, which significantly compromises the quality of life for cancer patients.[46] We propose a tissue engineering strategy to restore salivary gland function using primary epithelial cells isolated from the patient prior to radiation treatment and cell-permissive and cell-instructive synthetic matrices.[47] We have successfully isolated hS/PCs from human parotid glands; these cells can be readily expanded in culture. Compared to the parent tissue, hS/PCs exhibit increased expression of progenitor markers (*KRT5, KRT14, MYC, ETV4, ETV5*) and decreased expression of differentiation markers (acinar: *MIST1/BHLHA15* and *AMY1A;* ductal: *KRT19* and *TFCP2L1*).[20] Previously, we reported a 3D culture of hS/PCs in HA gels with or without integrin binding peptides, but not MMP-degradable.[19, 20, 22] A requisite for the growth and 3D self-assembly of hS/PCs is the usage of soft and compliant matrices with G' of 35-104 Pa. Multicellular structures evolved in these gels are spherical and tight; although cells expressed certain progenitor markers, KIT level was low.

In this work, we took advantage of the Michael-type addition reaction between thiol and maleimide to fabricate HA hydrogels with a consistent display of the integrin-binding peptide (RGDSP), comparable mechanical properties, but varying susceptibility to MMP-mediated degradation. The hydrogel matrix has a stiffness comparable to that of murine embryonic salivary glands.[48] Over the course of the 15 days, all three types of gel constructs remained structurally sound; we did not see obvious gel fragmentation and a significant increase in fluidicity. hS/PCs encapsulated in the HA hydrogels are viable and proliferative, forming multicellular spheroids as early as day 3. 0DEG gels promoted the formation of circular and tight hS/PCs assemblies. Incorporating protease degradability promoted the development of irregularly shaped structures.

To form multicellular structures in a non-degradable nano-porous matrix, hS/PCs must push away the HA chains to accommodate their increasing volume.[19] As a result of this

displacement, the HA matrix reciprocally increases a compressive, YAP-deactivating pressure against the cells. Under this condition, a sphere is the most energetically favourable shape.[49, 50] When encapsulated in a MMP-degradable matrix, hS/PCs can expand and assemble freely as the surrounding covalent cage is partially loosened by cell-secreted enzymes. As a result, these matrices permit more intimate cell-matrix interactions, thereby stimulating the rapid expansion of structures that deviate from the perfect spherical shape. It is reported that an imbalance in cell-cell and cell-matrix forces promotes salivary gland branching morphogenesis.[51] The non-spherical structures observed in the 50/100DEG hydrogels could arise from the build-up of dissimilar cell-matrix tension along the spheroids as MMP-mediated degradation began weakening areas of the hydrogel near the spheroids. In agreement with prior report,[14] hS/PCs in degradable matrices also proliferated more than those in non-degradable controls.

In addition to cell-ECM interactions, the establishment of cell-cell adhesions is critical to the maintenance of epithelial functions.[52] We demonstrate that β-catenin is localized to the cell-cell junctions under various culture conditions. Moreover, in 50DEG hydrogels, we observed strong β-catenin staining on the basal side. In 0DEG gels, some spheroids showed basal staining for β-catenin. The presence of β-catenin facing the ECM may indicate the polarization of spheroids,[53, 54] which is necessary for epithelial morphogenesis.[55] E-cadherin recruits β-catenin and helps anchor it to the basolateral membrane. Previous studies suggest that MMP/TIMP activity affects E-cadherin and β-catenin stability.[56, 57] Matrix degradation alters cell-matrix interaction, thus can affect pathways involved in β-catenin regulation and basal localization of β-catenin. However, we performed immunocytochemistry for GM130 (a polarity marker) and did not observe the apical localization of GM130 in either of the hydrogels, suggesting the spheroids were not correctly polarized (Figure S17). Future studies will identify necessary ECM cues to promote hS/PC polarization.

The irregularly shaped structures developed in 100DEG gels implies active matrix remodeling. IVIS imaging of cellular constructs made using fluorescently labelled hydrogels unambiguously confirmed matrix degradation in 50DEG and 100DEG during *in vitro* culture

(Figure S18). The GIW crosslinker used here is susceptible to degradation by MMP1,[45] MMP2,[45] MMP9,[45] and MMP14.[58] In response, cellular secretion of MMP1 and active collagenase, as well as the expression of *TIMP3,* correlate positively with matrix degradability. It is known that TIMP1 inhibits MMP1, TIMP2 inhibits MMP2 better than TIMP1,[59] and TIMP3 inhibits all MMPs.[60] Because a proper balance between MMPs and TIMPs is necessary for tissue morphogenesis,[60, 61] it is not surprising that gain or loss-of-function of MMPs and TIMPs results in defects in branched organs.[43, 62] The ECM at the end bud tip is thinner than the cleft region and ducts, indicating that MMPs are needed to cleave the ECM at the invasive front so that cells can proliferate, migrate, and invade the surrounding mesenchyme.[63]

Our tissue engineering approach aims to reconstitute and expand the stem/progenitor cell population in 3D in a tissue-mimetic configuration. Here, we show that the susceptibility of the HA gels to MMP degradation regulates the expression of key salivary gland stem cell markers. KRT5 and KRT14 are intermediate filaments,[64] and KRT5/KRT14+ progenitor cells contribute to specialized acinar, ductal, and myoepithelial cells in the gland.[27, 65] Salivary gland growth and regeneration also require CD44+ stem cells.[66, 67] Although the gene expression of *KRT14* did not change significantly across different hydrogel conditions, *KRT5* expression was sensitive to matrix composition, with the highest level detected in 50DEG cultures. CD44 expression was maintained consistently in 0DEG, 50DEG, and 100DEG hydrogels, both at the mRNA and protein levels.

Another key stem cell marker for the salivary gland is KIT. KIT, along with FGFR2b signaling, is reported to regulate progenitor expansion during salivary gland organogenesis.[27] KIT is found in the initial endbud formed in the embryonic salivary gland.[27] Its expression increased in the distal end bud as the branching morphogenesis occurred and the endbud and ducts increased in number.[27] KIT+ cells are among the most potent stem cells in the salivary gland, and as few as 500 KIT+ human salivary gland cells have been shown to improve salivary gland function following radiation in a mouse model.[25] However, the number of KIT+ cells diminishes with age, thus, the regenerative capacity of adult salivary gland is limited.[68, 69]

Previously, we show that *KIT* expression was significantly diminished in tissue-derived hS/PCs.[20] Although culturing hS/PCs in non-degradable HA hydrogel led to an increase in *KIT* expression, the level was still significantly lower compared to the human parotid gland.[20] Here, we discovered that hydrogels engineered with protease degradability enhanced the development of KIT+ cells. Incorporating MMP degradability resulted in up to 50- and 5-fold increase in KIT expression at the gene and the protein level, respectively. Our findings are robust and applicable to cells derived from donors of varying ages. This is a critical discovery as in previous studies, KIT-positive cells were difficult to maintain in vitro.[24] Additionally, we found that protease degradability increased the expression of the stem cell markers *ETV4* and *ETV5*. Our findings are supported by previous literature reporting that MAPK-ETV signaling supports the expansion of KIT progenitors in the mouse submandibular gland.[70] While we did not conduct mechanistic investigations, we speculate that hydrogel proteolytic degradation may help to sustain ETV signaling upstream of KIT. Taken together, our results indicate that the maintenance of the salivary gland stem/progenitor cells requires the synthetic matrices to be susceptible to MMP degradation.

Because radiation treatment irreversibly damages the differentiated acinar cells, our bioengineering approach further targets the enrichment of pro-acinar progenitor cells with secretory capabilities. Because the differentiation of the precursor cell is influenced by the changes in the extracellular microenvironment, we inquired whether MMP-mediated matrix remodeling triggers lineage commitment. In our 3D cultures, we observe a significant increase in amylase expression, both at the gene and the protein levels, when the synthetic matrices were MMP degradable. The expression of *AQP5, AQP3,* and *SLC12A2* was the highest in 50DEG cultures, although a significant difference was only detected for *AQP5* and *SLC12A2*. In agreement with observations, using mouse salivary gland cells, Shubin et al. showed that hydrogel degradability regulates the expression of acinar markers.[14]

In summary, we cultured hS/PCs in HA-based hydrogels with full (100DEG), partial (50DEG), or zero (0DEG) MMP degradability. While 0DEG gels promoted the development of tight spheroids, the degradable counterparts facilitated the establishment of multicellular

structures that are larger, irregularly shaped, and occasionally lobular. When cultured in 50DEG and 100DEG gels, hS/PCs expressed higher levels of stem/progenitor markers, as well as differentiated acinar markers. Future studies will aim to assess if hS/PCs cultured in gels with protease degradability have increased regenerative ability in appropriate animal models.

CONCLUSION

To develop an implantable salivary gland construct for the treatment of radiation-induced xerostomia, we cultured primary hS/PCs in RGD-conjugated HA hydrogels with comparable stiffness but a variable degree of proteolytic degradability. At the transcript level, we observed a significant increase in the expression of stem/progenitor markers *KIT* and *KRT5*, as well as acinar markers *AMY*, *SLC12A2*, and *AQP5* in 50DEG and 100DEG gels. Western blot analyses confirmed a significant increase in KIT expression in 50DEG and 100DEG hydrogels on day 15. Characterization by immunocytochemistry showed positive staining for stem cell markers KIT, K5, and CD44 in all the hydrogels, and positive staining for acinar marker α-amylase in 50DEG and 100DEG matrices. Collectively, we show that cell-mediated matrix degradability is necessary for the maintenance of a pro-acinar progenitor phenotype. This work represents a first step toward developing an engineered salivary gland.

SUPPORTING INFORMATION:

Chromatography/spectroscopy characterization of hydrogel precursors; Analysis of gelation kinetics and hydrogel stiffness; Fluorescent images of constructs treated with secondary antibody only; Individual stacks used to construct maximum intensity projections for day 15 images in Figure 2B and 3A; Hoechst 33342 staining for determining cell numbers; IVIS imaging of cell-laden hydrogels at day 1 and day 15; Original Western blot results, *KIT* expression by cells isolated from a 70-year-old patient; Quantification of amylase content; Immunofluorescence showing the distribution of polarity marker GM130; List of qPCR primers.

ACKNOWLEDGEMENT

This work was supported in part by the National Institutes of Health (NIDCR R01 DE029655, NIDCD, R01DC014461), National Science Foundation (NSF, DMR 2243648), and Delaware Bioscience Center for Advanced Technology (DE-CAT 12A00448). Instrumentation support was made possible by NIH (S10 OD016361, P20 GM103446) and NSF (CHE-0840401, CHE-1229234, IIA-1301765) grants. The authors also acknowledge the use of facilities and instrumentation supported by NSF through the University of Delaware Materials Research Science and Engineering Center (DMR 2011824). Microscopy access was supported by grants from the NIH-NIGMS (P20 GM103446), the NSF (IIA-1301765), and the State of Delaware. We thank Drs. Jeffrey Caplan and Sylvain Le Marchand for their expert assistance in confocal imaging and image analysis. We thank Sanofi/Genzyme for generously providing HA.

DATA AVAILABILITY

As part of an ongoing study, the raw/processed data required to reproduce these findings are available from the corresponding author on reasonable request.

REFERENCES

(1) Mody, M. D.; Rocco, J. W.; Yom, S. S.; Haddad, R. I.; Saba, N. F. Head and Neck Cancer. *Lancet* **2021**, *398* (10318), 2289–2299. DOI: 10.1016/s0140-6736(21)01550-6.

(2) Siegel, R. L.; Miller, K. D.; Fuchs, H. E.; Jemal, A. Cancer Statistics, 2022. *CA Cancer J. Clin.* **2022**, *72* (1), 7–33. DOI: 10.3322/caac.21708.

(3) Alterio, D.; Marvaso, G.; Ferrari, A.; Volpe, S.; Orecchia, R.; Jereczek-Fossa, B. A. Modern Radiotherapy for Head and Neck Cancer. *Semin. Oncol.* **2019**, *46* (3), 233–245. DOI: 10.1053/j.seminoncol.2019.07.002.

(4) Sheikh, K.; Lee, S. H.; Cheng, Z.; Lakshminarayanan, P.; Peng, L.; Han, P.; McNutt, T. R.; Quon, H.; Lee, J. Predicting Acute Radiation Induced Xerostomia in Head and Neck Cancer Using MR and CT Radiomics of Parotid and Submandibular Glands. *Radiat. Oncol.* **2019**, *14* (1), 131. DOI: 10.1186/s13014-019-1339-4.

(5) Deasy, J. O.; Moiseenko, V.; Marks, L.; Chao, K. S. C.; Nam, J.; Eisbruch, A. Radiotherapy Dose-Volume Effects on Salivary Gland Function. *Int. J. Radiat. Oncol. Biol. Phys.* **2010**, *76* (3 Suppl), S58-63. DOI: 10.1016/j.ijrobp.2009.06.090.

(6) Jasmer, K. J.; Gilman, K. E.; Muñoz Forti, K.; Weisman, G. A.; Limesand, K. H. Radiation-Induced Salivary Gland Dysfunction: Mechanisms, Therapeutics and Future Directions. *J. Clin. Med.* **2020**, *9* (12), 4095. DOI: 10.3390/jcm9124095.

(7) Lombaert, I. M. A.; Brunsting, J. F.; Wierenga, P. K.; Kampinga, H. H.; de Haan, G.; Coppes, R. P. Cytokine Treatment Improves Parenchymal and Vascular Damage of Salivary Glands after Irradiation. *Clin. Cancer Res.* **2008**, *14* (23), 7741–7750. DOI: 10.1158/1078-0432.CCR-08-1449.

(8) Lombaert, I. M. A.; Patel, V. N.; Jones, C. E.; Villier, D. C.; Canada, A. E.; Moore, M. R.; Berenstein, E.; Zheng, C.; Goldsmith, C. M.; Chorini, J. A.; Martin, D.; Zourelias, L.; Trombetta, M. G.; Edwards, P. C.; Meyer, K.; Ando, D.; Passineau, M. J.; Hoffman, M. P. CERE-120 Prevents Irradiation-Induced Hypofunction and Restores Immune Homeostasis in Porcine Salivary Glands. *Mol. Ther. Methods Clin. Dev.* **2020**, *18*, 839–855. DOI: 10.1016/j.omtm.2020.07.016.

(9) Konings, A. W. T.; Coppes, R. P.; Vissink, A. On the Mechanism of Salivary Gland Radiosensitivity. *Int. J. Radiat. Oncol. Biol. Phys.* **2005**, *62* (4), 1187–1194. DOI: 10.1016/j.ijrobp.2004.12.051.

(10) Stankeviciene, I.; Puriene, A.; Mieliauskaite, D.; Stangvaltaite-Mouhat, L.; Aleksejuniene, J. Detection of Xerostomia, Sicca, and Sjogren's Syndromes in a National Sample of Adults. *BMC Oral Health* **2021**, *21* (1), 552. DOI: 10.1186/s12903-021-01917-1.

(11) Bonnans, C.; Chou, J.; Werb, Z. Remodelling the Extracellular Matrix in Development and Disease. *Nat. Rev. Mol. Cell Biol.* **2014**, *15* (12), 786–801. DOI: 10.1038/nrm3904.

(12) Liu, X.; Sun, Q.; Wang, Q.; Hu, C.; Chen, X.; Li, H.; Czajkowsky, D. M.; Shao, Z. Epithelial Cells in 2D and 3D Cultures Exhibit Large Differences in Higher-Order Genomic Interactions. *Genomics Proteomics Bioinformatics* **2022**, *20* (1), 101–109. DOI: 10.1016/j.gpb.2020.06.017.

(13) Nerger, B. A.; Nelson, C. M. 3D Culture Models for Studying Branching Morphogenesis in the Mammary Gland and Mammalian Lung. *Biomaterials* **2019**, *198*, 135–145. DOI: 10.1016/j.biomaterials.2018.08.043.

(14) Shubin, A. D.; Felong, T. J.; Schutrum, B. E.; Joe, D. S. L.; Ovitt, C. E.; Benoit, D. S. W. Encapsulation of Primary Salivary Gland Cells in Enzymatically Degradable Poly(Ethylene Glycol) Hydrogels Promotes Acinar Cell Characteristics. *Acta Biomater.* **2017**, *50*, 437–449. DOI: 10.1016/j.actbio.2016.12.049.

(15) Shubin, A. D.; Felong, T. J.; Graunke, D.; Ovitt, C. E.; Benoit, D. S. W. Development of Poly(Ethylene Glycol) Hydrogels for Salivary Gland Tissue Engineering Applications. *Tissue Eng. Part A* **2015**, *21* (11–12), 1733–1751. DOI: 10.1089/ten.TEA.2014.0674.

(16) Burford-Mason, A. P.; Dardick, I.; MacKay, A. Collagen Gel Cultures of Normal Salivary Gland: Conditions for Continued Proliferation and Maintenance of Major Cell Phenotypes in Vitro: Conditions for Continued Proliferation and Maintenance of Major Cell Phenotypes in Vitro. *Laryngoscope* **1994**, *104* (3 Pt 1), 335–340. DOI: 10.1288/00005537-199403000-00016.

(17) Jorgensen, M.; Ramesh, P.; Toro, M.; Evans, E.; Moskwa, N.; Zhang, X.; Sharfstein, S. T.; Larsen, M.; Xie, Y. Alginate Hydrogel Microtubes for Salivary Gland Cell Organization

and Cavitation. *Bioengineering (Basel)* **2022**, *9* (1), 38. DOI: 10.3390/bioengineering9010038.

(18) Dos Santos, H. T.; Nam, K.; Brown, C. T.; Dean, S. M.; Lewis, S.; Pfeifer, C. S.; Lei, P.; Petris, M. J.; Andreadis, S. T.; Baker, O. J. Trimers Conjugated to Fibrin Hydrogels Promote Salivary Gland Function. *J. Dent. Res.* **2021**, *100* (3), 268–275. DOI: 10.1177/0022034520964784.

(19) Fowler, E. W.; Ravikrishnan, A.; Witt, R. L.; Pradhan-Bhatt, S.; Jia, X. RGDSP-Decorated Hyaluronate Hydrogels Facilitate Rapid 3D Expansion of Amylase-Expressing Salivary Gland Progenitor Cells. *ACS Biomater. Sci. Eng.* **2021**, *7* (12), 5749–5761. DOI: 10.1021/acsbiomaterials.1c00745.

(20) Srinivasan, P. P.; Patel, V. N.; Liu, S.; Harrington, D. A.; Hoffman, M. P.; Jia, X.; Witt, R. L.; Farach-Carson, M. C.; Pradhan-Bhatt, S. Primary Salivary Human Stem/Progenitor Cells Undergo Microenvironment-Driven Acinar-like Differentiation in Hyaluronate Hydrogel Culture. *Stem Cells Transl. Med.* **2017**, *6* (1), 110–120. DOI: 10.5966/sctm.2016-0083.

(21) Xu, X.; Jha, A. K.; Harrington, D. A.; Farach-Carson, M. C.; Jia, X. Hyaluronic Acid-Based Hydrogels: From a Natural Polysaccharide to Complex Networks. *Soft Matter* **2012**, *8* (12), 3280–3294. DOI: 10.1039/C2SM06463D.

(22) Ozdemir, T.; Fowler, E. W.; Liu, S.; Harrington, D. A.; Witt, R. L.; Farach-Carson, M. C.; Pradhan-Bhatt, S.; Jia, X. Tuning Hydrogel Properties to Promote the Assembly of Salivary Gland Spheroids in 3D. *ACS Biomater. Sci. Eng.* **2016**, *2* (12), 2217–2230. DOI: 10.1021/acsbiomaterials.6b00419.

(23) Rocchi, C.; Barazzuol, L.; Coppes, R. P. The Evolving Definition of Salivary Gland Stem Cells. *NPJ Regen. Med.* **2021**, *6* (1), 4. DOI: 10.1038/s41536-020-00115-x.

(24) Nanduri, L. S. Y.; Lombaert, I. M. A.; van der Zwaag, M.; Faber, H.; Brunsting, J. F.; van Os, R. P.; Coppes, R. P. Salisphere Derived C-Kit+ Cell Transplantation Restores Tissue Homeostasis in Irradiated Salivary Gland. *Radiother. Oncol.* **2013**, *108* (3), 458–463. DOI: 10.1016/j.radonc.2013.05.020.

(25) Lombaert, I.; Movahednia, M. M.; Adine, C.; Ferreira, J. N. Concise Review: Salivary Gland Regeneration: Therapeutic Approaches from Stem Cells to Tissue Organoids. *Stem Cells* **2017**, *35* (1), 97–105. DOI: 10.1002/stem.2455.

(26) Emmerson, E.; Knox, S. M. Salivary Gland Stem Cells: A Review of Development, Regeneration and Cancer. *Genesis* **2018**, *56* (5), e23211. DOI: 10.1002/dvg.23211.

(27) Lombaert, I. M. A.; Abrams, S. R.; Li, L.; Eswarakumar, V. P.; Sethi, A. J.; Witt, R. L.; Hoffman, M. P. Combined KIT and FGFR2b Signaling Regulates Epithelial Progenitor Expansion during Organogenesis. *Stem Cell Reports* **2013**, *1* (6), 604–619. DOI: 10.1016/j.stemcr.2013.10.013.

(28) Madl, C. M.; LeSavage, B. L.; Dewi, R. E.; Dinh, C. B.; Stowers, R. S.; Khariton, M.; Lampe, K. J.; Nguyen, D.; Chaudhuri, O.; Enejder, A.; Heilshorn, S. C. Maintenance of Neural Progenitor Cell Stemness in 3D Hydrogels Requires Matrix Remodelling. *Nat. Mater.* **2017**, *16* (12), 1233–1242. DOI: 10.1038/nmat5020.

(29) Smith, L. R.; Cho, S.; Discher, D. E. Stem Cell Differentiation Is Regulated by Extracellular Matrix Mechanics. *Physiology (Bethesda)* **2018**, *33* (1), 16–25. DOI: 10.1152/physiol.00026.2017.

(30) Feng, Q.; Zhu, M.; Wei, K.; Bian, L. Cell-Mediated Degradation Regulates Human Mesenchymal Stem Cell Chondrogenesis and Hypertrophy in MMP-Sensitive Hyaluronic Acid Hydrogels. *PLoS One* **2014**, *9* (6), e99587. DOI: 10.1371/journal.pone.0099587.

(31) Khetan, S.; Guvendiren, M.; Legant, W. R.; Cohen, D. M.; Chen, C. S.; Burdick, J. A. Degradation-Mediated Cellular Traction Directs Stem Cell Fate in Covalently Crosslinked Three-Dimensional Hydrogels. *Nat. Mater.* **2013**, *12* (5), 458–465. DOI: 10.1038/nmat3586.

(32) Zerdoum, A. B.; Fowler, E. W.; Jia, X. Induction of Fibrogenic Phenotype in Human Mesenchymal Stem Cells by Connective Tissue Growth Factor in a Hydrogel Model of Soft Connective Tissue. *ACS Biomater. Sci. Eng.* **2019**, *5* (9), 4531–4541. DOI: 10.1021/acsbiomaterials.9b00425.

(33) Jia, H.; Zhao, J.-Z.; Jin, F.-Y.; Pu, W.-F.; Li, Y.-M.; Li, K.-X.; Li, J.-M. New Insights into the Gelation Behavior of Polyethyleneimine Cross-Linking Partially Hydrolyzed Polyacrylamide Gels. *Ind. Eng. Chem. Res.* **2012**, *51* (38), 12155–12166. DOI: 10.1021/ie301818f.

(34) Pradhan-Bhatt, S.; Harrington, D. A.; Duncan, R. L.; Jia, X.; Witt, R. L.; Farach-Carson, M. C. Implantable Three-Dimensional Salivary Spheroid Assemblies Demonstrate Fluid and Protein Secretory Responses to Neurotransmitters. *Tissue Eng. Part A* **2013**, *19* (13–14), 1610–1620. DOI: 10.1089/ten.tea.2012.0301.

(35) Pradhan, S.; Zhang, C.; Jia, X.; Carson, D. D.; Witt, R.; Farach-Carson, M. C. Perlecan Domain IV Peptide Stimulates Salivary Gland Cell Assembly in Vitro. *Tissue Eng. Part A* **2009**, *15* (11), 3309–3320. DOI: 10.1089/ten.TEA.2008.0669.

(36) Nie, X.; Li, C.; Hu, S.; Xue, F.; Kang, Y. J.; Zhang, W. An Appropriate Loading Control for Western Blot Analysis in Animal Models of Myocardial Ischemic Infarction. *Biochem. Biophys. Rep.* **2017**, *12*, 108–113. DOI: 10.1016/j.bbrep.2017.09.001.

(37) Darling, N. J.; Hung, Y.-S.; Sharma, S.; Segura, T. Controlling the Kinetics of Thiol-Maleimide Michael-Type Addition Gelation Kinetics for the Generation of Homogenous Poly(Ethylene Glycol) Hydrogels. *Biomaterials* **2016**, *101*, 199–206. DOI: 10.1016/j.biomaterials.2016.05.053.

(38) Fowler, E. W.; van Venrooy, E. J.; Witt, R. L.; Jia, X. A TGFβR Inhibitor Represses Keratin-7 Expression in 3D Cultures of Human Salivary Gland Progenitor Cells. *Sci. Rep.* **2022**, *12* (1), 15008. DOI: 10.1038/s41598-022-19253-x.

(39) Freemont, A. J. Demystified ... Adhesion Molecules. *Mol. Pathol.* **1998**, *51* (4), 175–184. DOI: 10.1136/mp.51.4.175.

(40) Howard, S.; Deroo, T.; Fujita, Y.; Itasaki, N. A Positive Role of Cadherin in Wnt/β-Catenin Signalling during Epithelial-Mesenchymal Transition. *PLoS One* **2011**, *6* (8), e23899. DOI: 10.1371/journal.pone.0023899.

(41) Wang, B.; Qin, P.; Zhao, H.; Xia, T.; Wang, J.; Liu, L.; Zhu, L.; Xu, J.; Huang, C.; Shi, Y.; Du, Y. Substrate Stiffness Orchestrates Epithelial Cellular Heterogeneity with Controlled Proliferative Pattern via E-Cadherin/β-Catenin Mechanotransduction. *Acta Biomater.* **2016**, *41*, 169–180. DOI: 10.1016/j.actbio.2016.05.025.

(42) Raza, A.; Ki, C. S.; Lin, C.-C. The Influence of Matrix Properties on Growth and Morphogenesis of Human Pancreatic Ductal Epithelial Cells in 3D. *Biomaterials* **2013**, *34* (21), 5117–5127. DOI: 10.1016/j.biomaterials.2013.03.086.

(43) Page-McCaw, A.; Ewald, A. J.; Werb, Z. Matrix Metalloproteinases and the Regulation of Tissue Remodelling. *Nat. Rev. Mol. Cell Biol.* **2007**, *8* (3), 221–233. DOI: 10.1038/nrm2125.

(44) Cabral-Pacheco, G. A.; Garza-Veloz, I.; Castruita-De la Rosa, C.; Ramirez-Acuña, J. M.; Perez-Romero, B. A.; Guerrero-Rodriguez, J. F.; Martinez-Avila, N.; Martinez-Fierro, M. L. The Roles of Matrix Metalloproteinases and Their Inhibitors in Human Diseases. *Int. J. Mol. Sci.* **2020**, *21* (24), 9739. DOI: 10.3390/ijms21249739.

(45) Patterson, J.; Hubbell, J. A. Enhanced Proteolytic Degradation of Molecularly Engineered PEG Hydrogels in Response to MMP-1 and MMP-2. *Biomaterials* **2010**, *31* (30), 7836–7845. DOI: 10.1016/j.biomaterials.2010.06.061.

(46) Goel, B.; Tiwari, A. K.; Pandey, R. K.; Singh, A. P.; Kumar, S.; Sinha, A.; Jain, S. K.; Khattri, A. Therapeutic Approaches for the Treatment of Head and Neck Squamous Cell Carcinoma-An Update on Clinical Trials. *Transl. Oncol.* **2022**, *21* (101426), 101426. DOI: 10.1016/j.tranon.2022.101426.

(47) Ozdemir, T.; Fowler, E. W.; Hao, Y.; Ravikrishnan, A.; Harrington, D. A.; Witt, R. L.; Farach-Carson, M. C.; Pradhan-Bhatt, S.; Jia, X. Biomaterials-Based Strategies for Salivary Gland Tissue Regeneration. *Biomater. Sci.* **2016**, *4* (4), 592–604. DOI: 10.1039/c5bm00358j.

(48) Mosier, A. P.; Peters, S. B.; Larsen, M.; Cady, N. C. Microfluidic Platform for the Elastic Characterization of Mouse Submandibular Glands by Atomic Force Microscopy. *Biosensors (Basel)* **2014**, *4* (1), 18–27. DOI: 10.3390/bios4010018.

(49) Taubenberger, A. V.; Girardo, S.; Träber, N.; Fischer-Friedrich, E.; Kräter, M.; Wagner, K.; Kurth, T.; Richter, I.; Haller, B.; Binner, M.; Hahn, D.; Freudenberg, U.; Werner, C.; Guck, J. 3D Microenvironment Stiffness Regulates Tumor Spheroid Growth and Mechanics via P21 and ROCK. *Adv. Biosyst.* **2019**, *3* (9), e1900128. DOI: 10.1002/adbi.201900128.

(50) Xia, P.; Gütl, D.; Zheden, V.; Heisenberg, C.-P. Lateral Inhibition in Cell Specification Mediated by Mechanical Signals Modulating TAZ Activity. *Cell* **2019**, *176* (6), 1379-1392.e14. DOI: 10.1016/j.cell.2019.01.019.

(51) Wang, S.; Matsumoto, K.; Lish, S. R.; Cartagena-Rivera, A. X.; Yamada, K. M. Budding Epithelial Morphogenesis Driven by Cell-Matrix versus Cell-Cell Adhesion. *Cell* **2021**, *184* (14), 3702-3716.e30. DOI: 10.1016/j.cell.2021.05.015.

(52) Baum, B.; Georgiou, M. Dynamics of Adherens Junctions in Epithelial Establishment, Maintenance, and Remodeling. *J. Cell Biol.* **2011**, *192* (6), 907–917. DOI: 10.1083/jcb.201009141.

(53) Chung, I.-M.; Enemchukwu, N. O.; Khaja, S. D.; Murthy, N.; Mantalaris, A.; García, A. J. Bioadhesive Hydrogel Microenvironments to Modulate Epithelial Morphogenesis. *Biomaterials* **2008**, *29* (17), 2637–2645. DOI: 10.1016/j.biomaterials.2008.03.008.

(54) Martín-Belmonte, F.; Yu, W.; Rodríguez-Fraticelli, A. E.; Ewald, A. J.; Werb, Z.; Alonso, M. A.; Mostov, K. Cell-Polarity Dynamics Controls the Mechanism of Lumen Formation in Epithelial Morphogenesis. *Curr. Biol.* **2008**, *18* (7), 507–513. DOI: 10.1016/j.cub.2008.02.076.

(55) Roignot, J.; Peng, X.; Mostov, K. Polarity in Mammalian Epithelial Morphogenesis. *Cold Spring Harb. Perspect. Biol.* **2013**, *5* (2), a013789–a013789. DOI: 10.1101/cshperspect.a013789.

(56) Khokha, R.; Waterhouse, P.; Yagel, S.; Lala, P. K.; Overall, C. M.; Norton, G.; Denhardt, D. T. Antisense RNA-Induced Reduction in Murine TIMP Levels Confers Oncogenicity on Swiss 3T3 Cells. *Science* **1989**, *243* (4893), 947–950. DOI: 10.1126/science.2465572.

(57) Lochter, A.; Galosy, S.; Muschler, J.; Freedman, N.; Werb, Z.; Bissell, M. J. Matrix Metalloproteinase Stromelysin-1 Triggers a Cascade of Molecular Alterations That Leads to Stable Epithelial-to-Mesenchymal Conversion and a Premalignant Phenotype in Mammary Epithelial Cells. *J. Cell Biol.* **1997**, *139* (7), 1861–1872. DOI: 10.1083/jcb.139.7.1861.

(58) Bracher, M.; Bezuidenhout, D.; Lutolf, M. P.; Franz, T.; Sun, M.; Zilla, P.; Davies, N. H. Cell Specific Ingrowth Hydrogels. *Biomaterials* **2013**, *34* (28), 6797–6803. DOI: 10.1016/j.biomaterials.2013.05.057.

(59) Itoh, Y.; Ito, A.; Iwata, K.; Tanzawa, K.; Mori, Y.; Nagase, H. Plasma Membrane-Bound Tissue Inhibitor of Metalloproteinases (TIMP)-2 Specifically Inhibits Matrix Metalloproteinase 2 (Gelatinase A) Activated on the Cell Surface. *J. Biol. Chem.* **1998**, *273* (38), 24360–24367. DOI: 10.1074/jbc.273.38.24360.

(60) Fan, D.; Kassiri, Z. Biology of Tissue Inhibitor of Metalloproteinase 3 (TIMP3), and Its Therapeutic Implications in Cardiovascular Pathology. *Front. Physiol.* **2020**, *11*, 661. DOI: 10.3389/fphys.2020.00661.

(61) Gill, S. E.; Pape, M. C.; Leco, K. J. Tissue Inhibitor of Metalloproteinases 3 Regulates Extracellular Matrix--Cell Signaling during Bronchiole Branching Morphogenesis. *Dev. Biol.* **2006**, *298* (2), 540–554. DOI: 10.1016/j.ydbio.2006.07.004.

(62) Fata, J. E.; Werb, Z.; Bissell, M. J. Regulation of Mammary Gland Branching Morphogenesis by the Extracellular Matrix and Its Remodeling Enzymes. *Breast Cancer Res.* **2004**, *6* (1), 1–11. DOI: 10.1186/bcr634.

(63) Daley, W. P.; Yamada, K. M. ECM-Modulated Cellular Dynamics as a Driving Force for Tissue Morphogenesis. *Curr. Opin. Genet. Dev.* **2013**, *23* (4), 408–414. DOI: 10.1016/j.gde.2013.05.005.

(64) Abashev, T. M.; Metzler, M. A.; Wright, D. M.; Sandell, L. L. Retinoic Acid Signaling Regulates Krt5 and Krt14 Independently of Stem Cell Markers in Submandibular Salivary Gland Epithelium. *Dev. Dyn.* **2017**, *246* (2), 135–147. DOI: 10.1002/dvdy.24476.

(65) Knox, S. M.; Lombaert, I. M. A.; Reed, X.; Vitale-Cross, L.; Gutkind, J. S.; Hoffman, M. P. Parasympathetic Innervation Maintains Epithelial Progenitor Cells during Salivary Organogenesis. *Science* **2010**, *329* (5999), 1645–1647. DOI: 10.1126/science.1192046.

(66) Pradhan-Bhatt, S.; Harrington, D. A.; Duncan, R. L.; Farach-Carson, M. C.; Jia, X.; Witt, R. L. A Novel in Vivo Model for Evaluating Functional Restoration of a Tissue-Engineered Salivary Gland: In Vivo Model for Salivary Gland Regeneration. *Laryngoscope* **2014**, *124* (2), 456–461. DOI: 10.1002/lary.24297.

(67) Fonseca, I.; Moura Nunes, J. F.; Soares, J. Expression of CD44 Isoforms in Normal Salivary Gland Tissue: An Immunohistochemical and Ultrastructural Study. *Histochem. Cell Biol.* **2000**, *114* (6), 483–488. DOI: 10.1007/s004180000220.

(68) Feng, J.; van der Zwaag, M.; Stokman, M. A.; van Os, R.; Coppes, R. P. Isolation and Characterization of Human Salivary Gland Cells for Stem Cell Transplantation to Reduce Radiation-Induced Hyposalivation. *Radiother. Oncol.* **2009**, *92* (3), 466–471. DOI: 10.1016/j.radonc.2009.06.023.

(69) Maimets, M.; Bron, R.; de Haan, G.; van Os, R.; Coppes, R. P. Similar Ex Vivo Expansion and Post-Irradiation Regenerative Potential of Juvenile and Aged Salivary Gland Stem Cells. *Radiother. Oncol.* **2015**, *116* (3), 443–448. DOI: 10.1016/j.radonc.2015.06.022.

(70) Patel, V. N.; Lombaert, I. M. A.; Cowherd, S. N.; Shworak, N. W.; Xu, Y.; Liu, J.; Hoffman, M. P. Hs3st3-Modified Heparan Sulfate Controls KIT+ Progenitor Expansion by Regulating 3-O-Sulfotransferases. *Dev. Cell* **2014**, *29* (6), 662–673. DOI: 10.1016/j.devcel.2014.04.024.

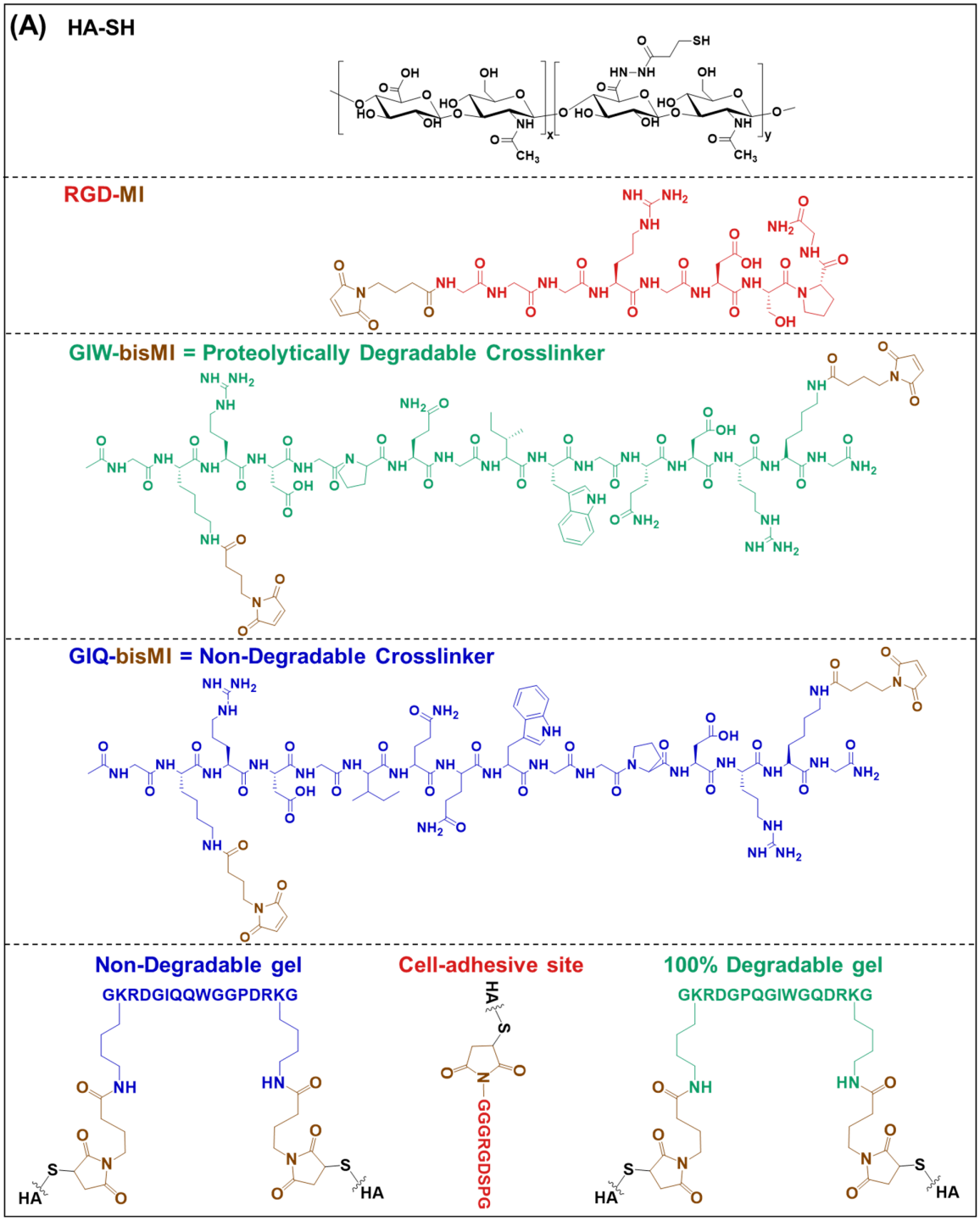
(A) HA-SH
RGD-MI
GIW-bisMI = Proteolytically Degradable Crosslinker
GIQ-bisMI = Non-Degradable Crosslinker
Non-Degradable gel
GKRDGIQQWGGPDRKG
Cell-adhesive site
GGGRGDSPG
100% Degradable gel
GKRDGPQGIWGQDRKG

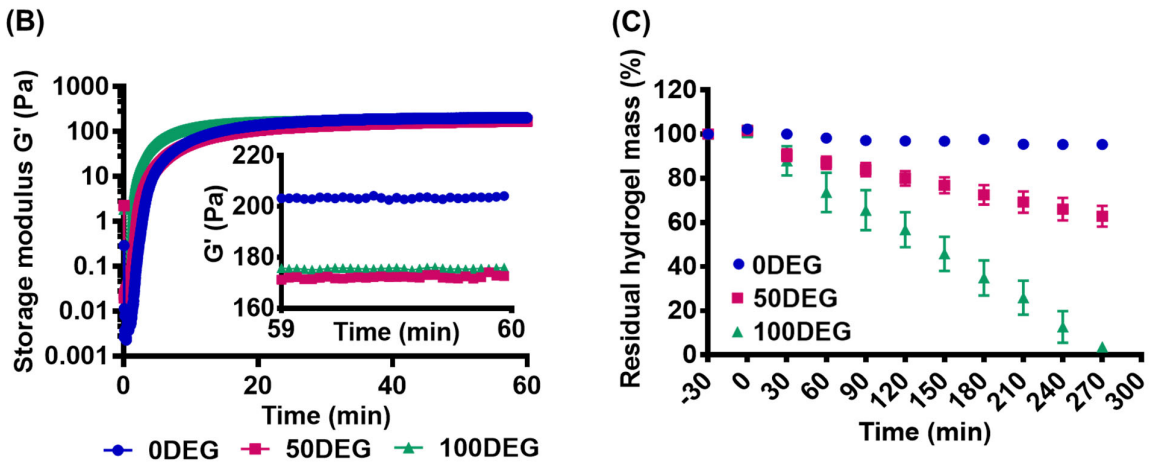

Figure 1. Synthesis and characterization of RGD-decorated HA gels with varying susceptibility to MMP-mediated degradation. **(A)** Hydrogels were established via Michael-type addition reaction using thiolated HA (HA-SH), maleimide-functionalized cell adhesive peptide (RGD-MI), and bis-maleimide crosslinkers that are MMP-degradable (GIW-bisMI) or non-degradable (GIQ-bisMI). **(B)** Representative oscillatory shear rheometry results showing elastic modulus (G') as a function of time. Hydrogels prepared using varying amounts of GIW/GIQ-bisMI crosslinkers exhibited comparable G'. Analysis across three biological replicas did not reveal any significant differences in G' across the three hydrogel formulations. **(C)** Gravimetric characterization of hydrogel degradation by collagenase IV (100 U/mL). Collagenase IV solution was added at 30 min.

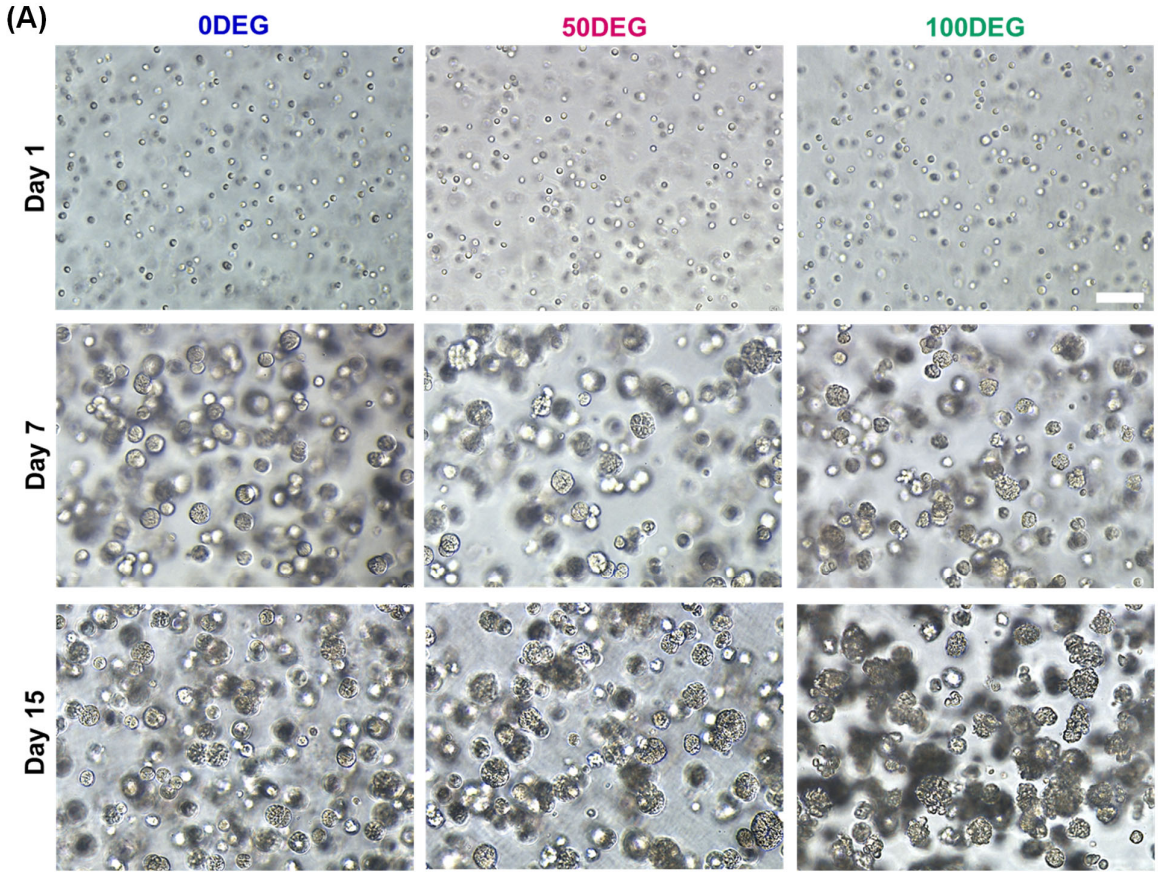
(A)
0DEG
50DEG
100DEG
Day 1
Day 7
Day 15

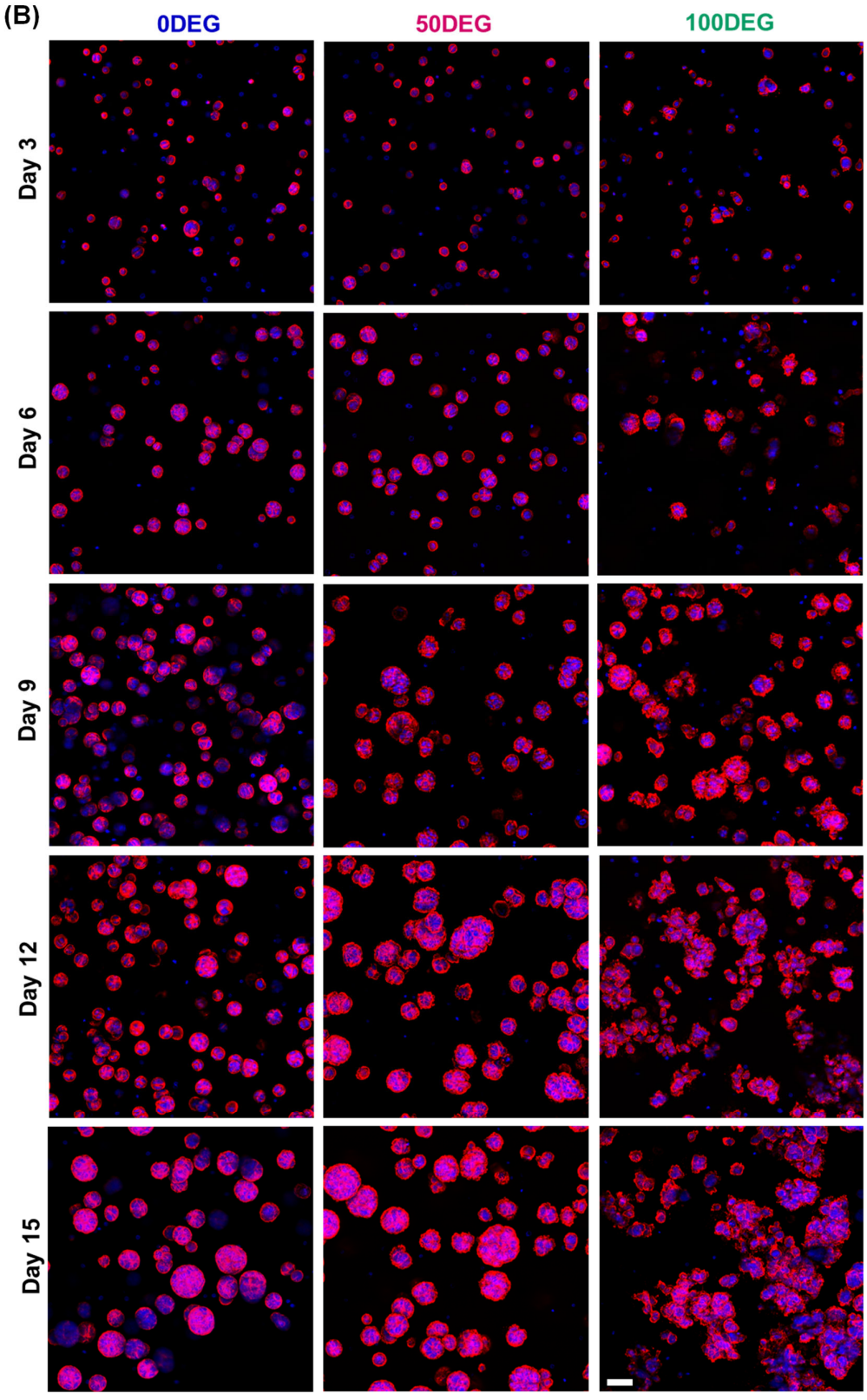
(B)
0DEG
50DEG
100DEG
Day 3
Day 6
Day 9
Day 12
Day 15

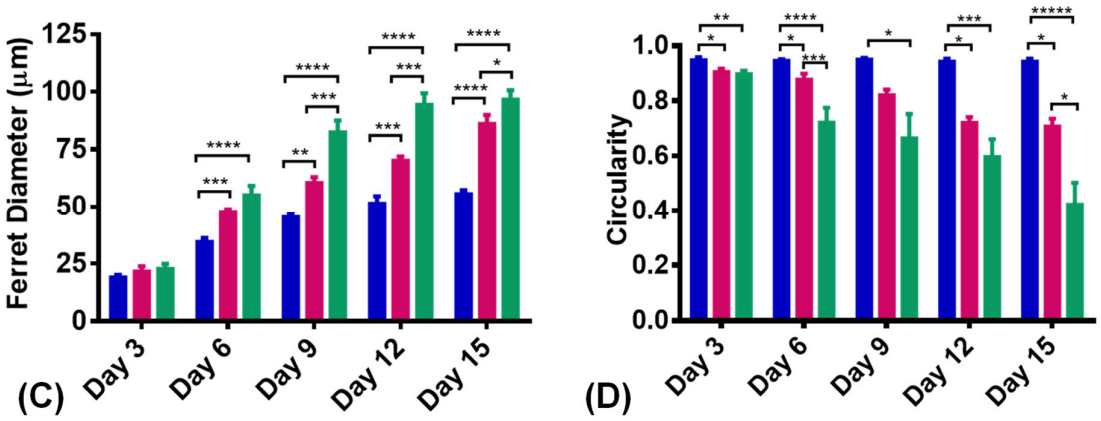

Figure 2. Characterization of the size and shape of multicellular hS/PC structures. **(A)** 3D growth of hS/PCs in gels with varying degradability as monitored using a brightfield microscope. Scale bar: 100 µm. (**B**) Representative maximum intensity projection of confocal z-stack (101.18 µm) images of hS/PC cultures on days 3-15. Cell nuclei were stained blue with Hoechst and F-actin was stained red by phalloidin. Scale bar: 50 µm. **(C-D)** Characterization of spheroid size and shape as Feret's diameter (C) and circularity (D). Analyses were performed using Hoechst/F-actin-stained confocal images. Error bars represent SEM in all cases. One-way ANOVA, followed by post hoc Tukey's test. * indicates $p < 0.05$, ** indicates $p < 0.01$, *** indicates $p < 0.005$, **** indicates $p < 0.001$, ***** indicates $p < 0.0001$ between 0DEG, 50DEG, and 100DEG at the same time point.

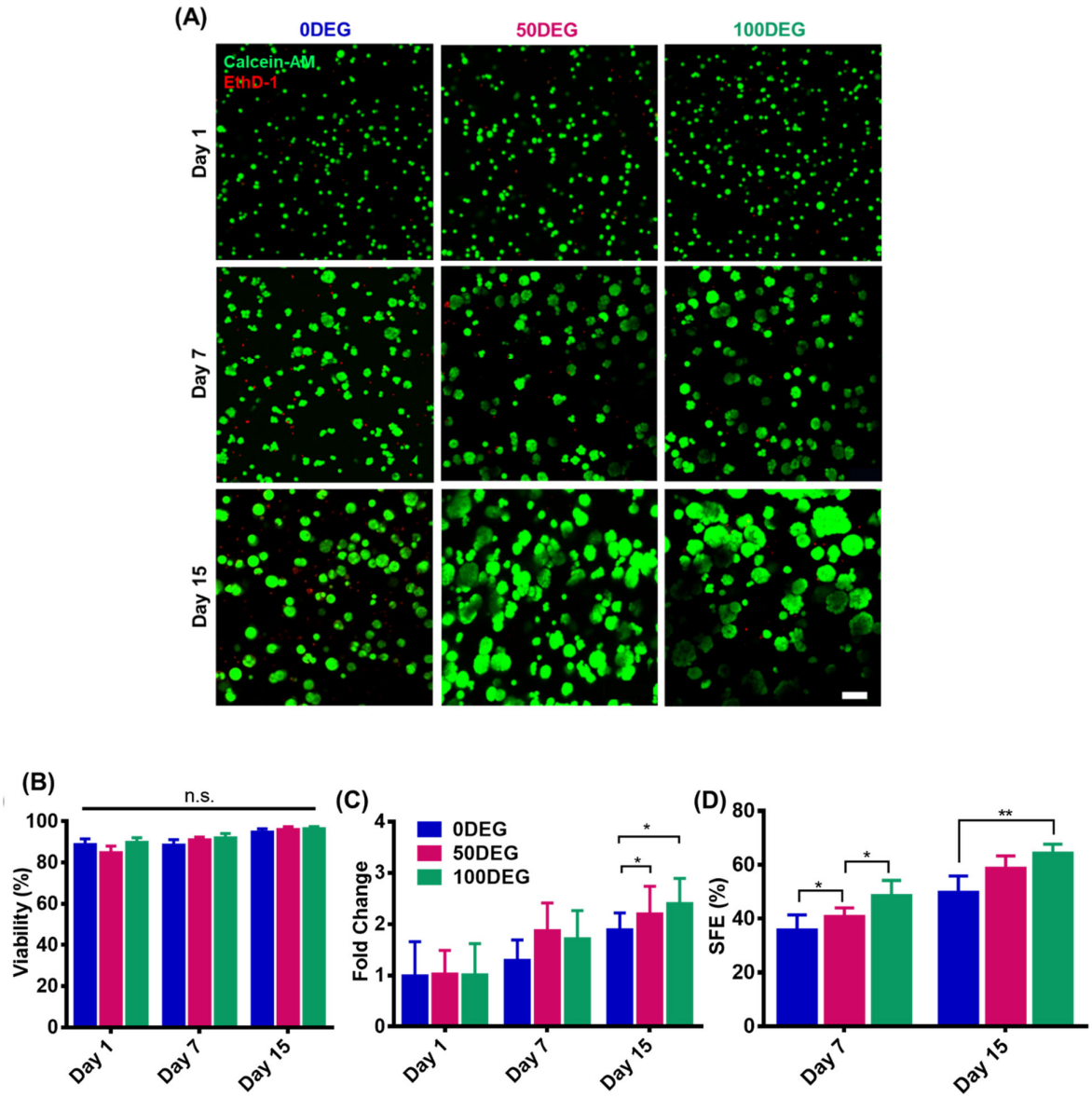

Figure 3. Effects of matrix degradability on cell viability (A), proliferation (B) and spheroid forming efficiency (SFE, C). **(A)** Representative confocal images of hS/PCs after live/dead staining. Live cells were stained green by calcein and dead cells were stained red by EthD-1. Scale bar: 100 μm. **(B)** Percent viable cells as a function of culture time and gel composition. Using ImageJ software, viability was determined by subtracting dead cells stained by EthD-1 from the total number of cells stained by Hoechst. **(C)** Effects of culture time and gel composition on hS/PC proliferation. Proliferation, as fold change, was determined by comparing the total number of viable cells on a given day to the total number of cells on day

1. **(D)** Effects of culture time and conditions on spheroid forming efficiency. Cell number on day 1 was determined from the Hoechst nuclear labeling. Spheroids were defined as structures with three or more calcein and Hoechst-stained cells that were close to each other. SFE is defined as the number of spheroids found at day 7 or 15 relative to the day 1 cell number. Error bars represent SEM in all cases. One-way ANOVAs were performed on (B-D) data sets, followed by post hoc Tukey's test. * indicates $p < 0.05$, ** indicates $p < 0.01$ between 0DEG, 50DEG, and 100DEG at the same time point.

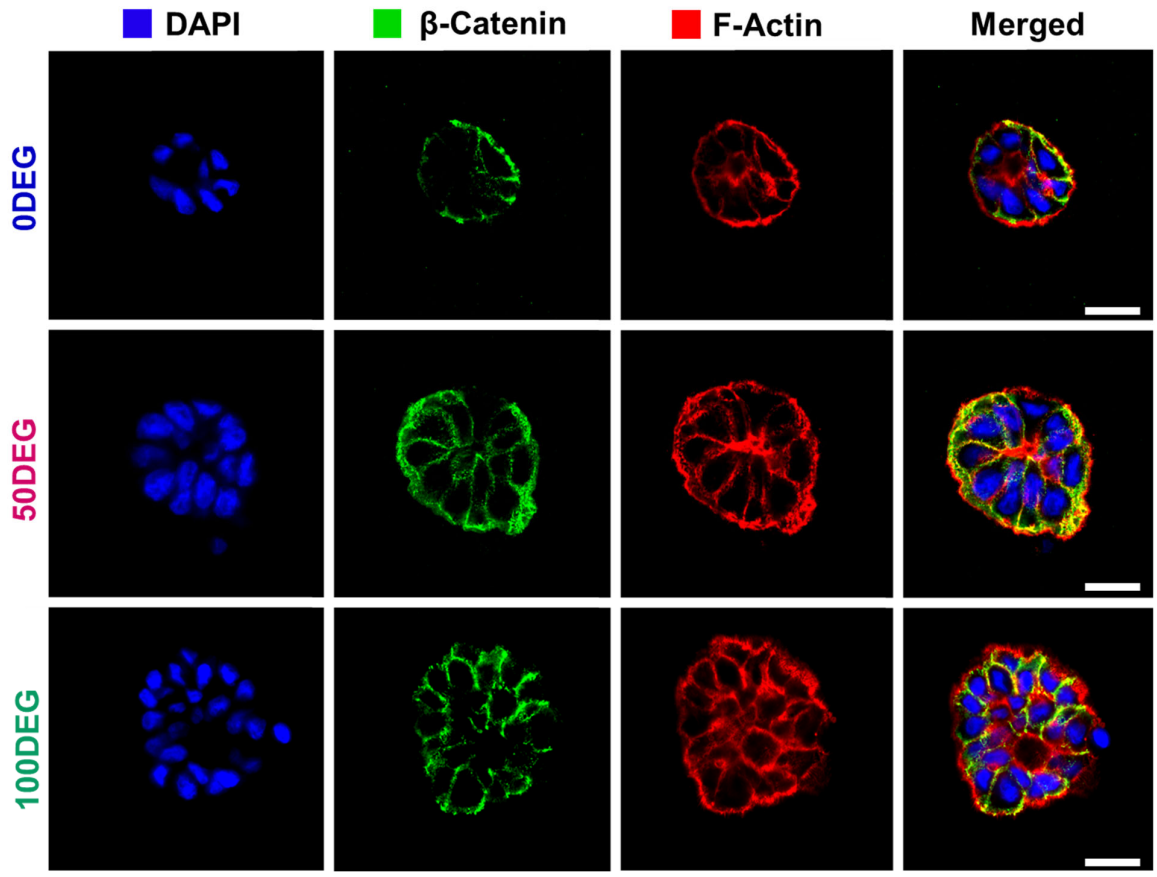

Figure 4. Characterization of β-catenin expression by day 15 hS/PC cultures by immunofluorescence. Hydrogel-derived hS/PC multicellular spheroids maintain cell-cell contacts as depicted by β-catenin staining. Scale bar: 20 μm.

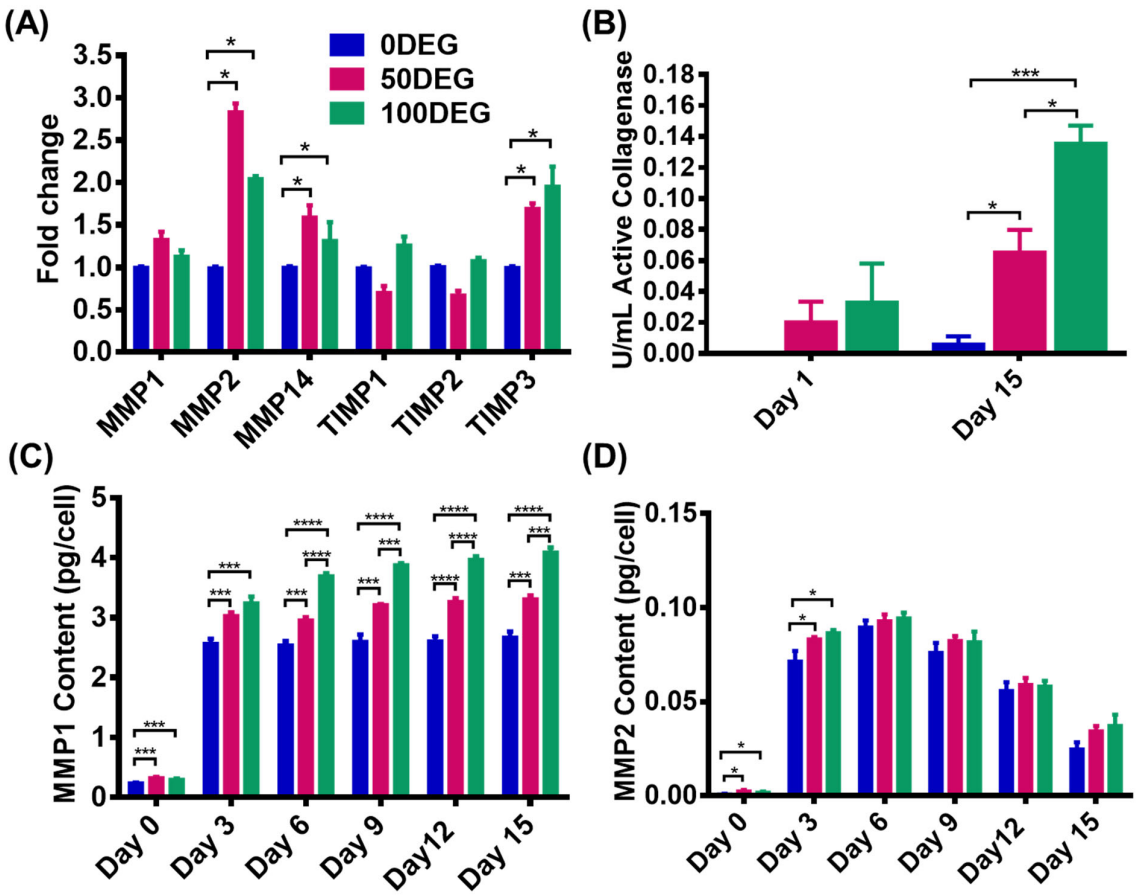

Figure 5. Characterization of protease expression by qPCR (A), Enzcheck assay (B), and ELISA (C-D). **(A)** qPCR analyses for the expression of MMPs and TIMPs by day 15 of cultures. *GAPDH* was used as the house keeping gene. **(B)** Active collagenase content in 0DEG, 50DEG, and 100DEG cultures on day 1 and day 15. **(C-D)** Cellular secretion of MMP1 (C) and 2 (D) on days 0 (5 h after encapsulation), 3, 6, 9, 12, 15 as quantified by ELISA. Error bars represent SEM in all cases. One-way ANOVAs were performed on all the data sets, followed by post hoc Tukey's test. * indicates $p < 0.05$, ** indicates $p < 0.01$, *** indicates $p < 0.005$, **** indicates $p < 0.001$ between 0DEG, 50DEG, and 100DEG at the same time point.

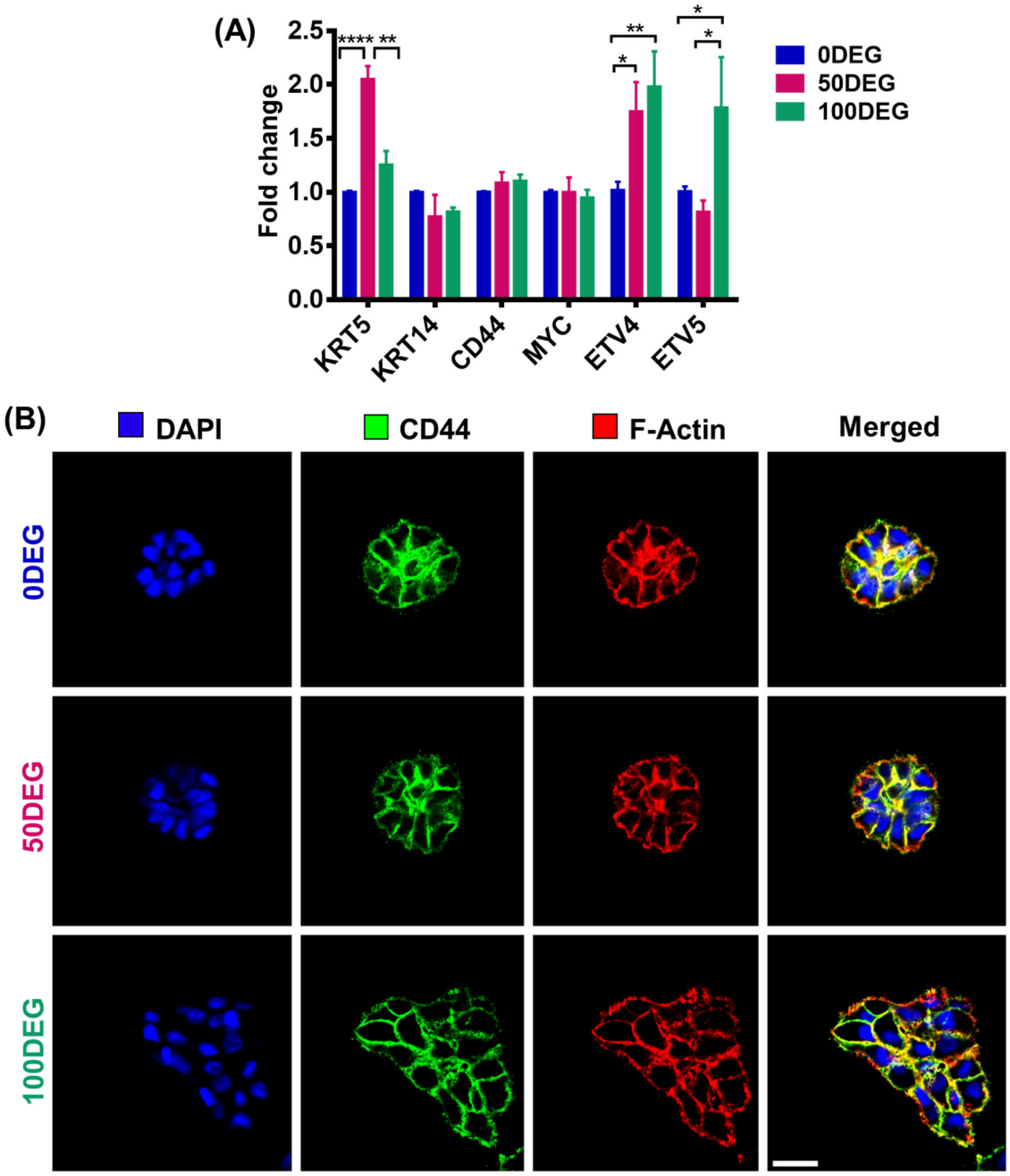
(A)
Fold change
2.5
2.0
1.5
1.0
0.5
0.0
****
**
*
**
*
*
0DEG
50DEG
100DEG
KRT5
KRT14
CD44
MYC
ETV4
ETV5
(B)
DAPI
CD44
F-Actin
Merged
0DEG
50DEG
100DEG

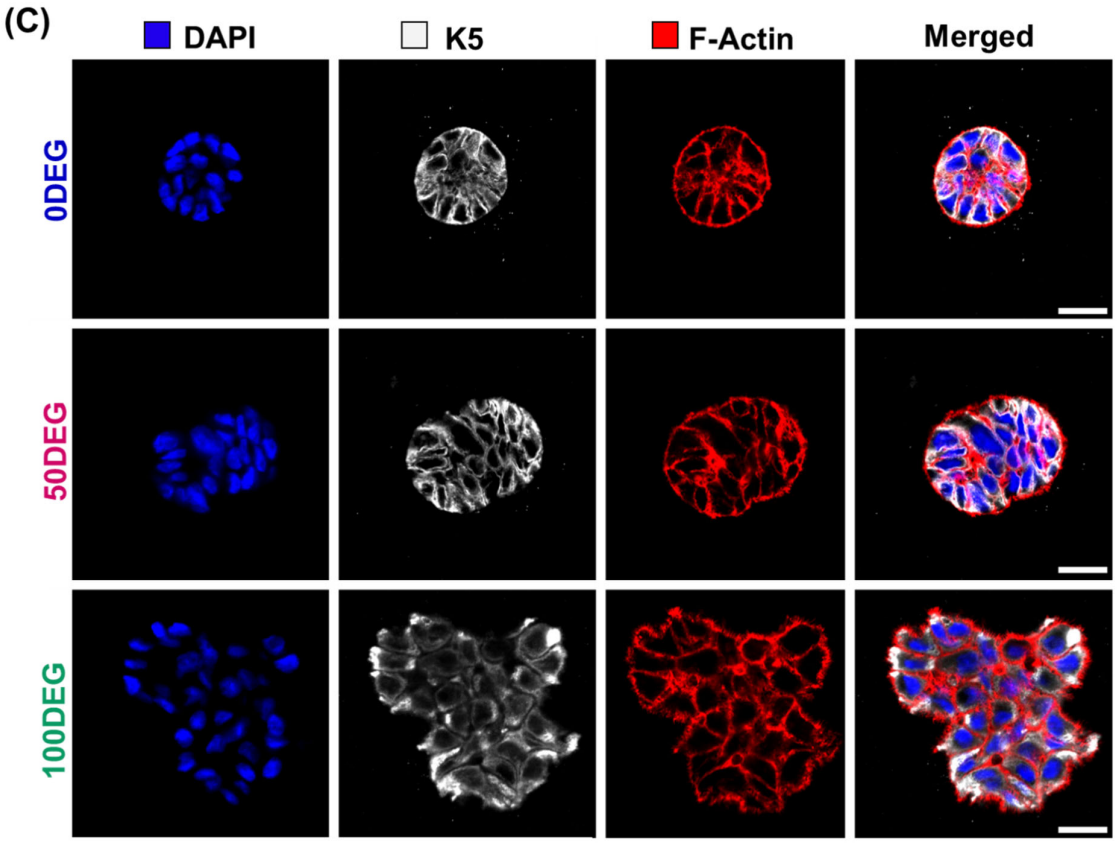

Figure 6. Characterization of the expression of stem/progenitor markers by qPCR (A) and immunofluorescence (B, C). **(A)** qPCR analyses of day 15 constructs for the expression of salivary gland progenitor (*KRT5*, *KRT14*), and stem cell markers (*CD44*, *MYC*, *EVT4/5*). *GAPDH* was used as the house keeping gene. Error bars represent SEM in all cases. One-way ANOVA, followed by post hoc Tukey's test. * indicates $p < 0.05$, ** indicates $p < 0.01$, *** indicates $p < 0.005$, **** indicates $p < 0.001$ between 0DEG, 50DEG, and 100DEG at the same time point. **(B)** Confocal images of day 15 constructs stained for CD44 (green), F-actin (red), and nuclei (blue). **(C)** Confocal images of day 15 constructs stained for K5 (white), F-actin (red), and nuclei (blue). Scale bar: 20 μm.

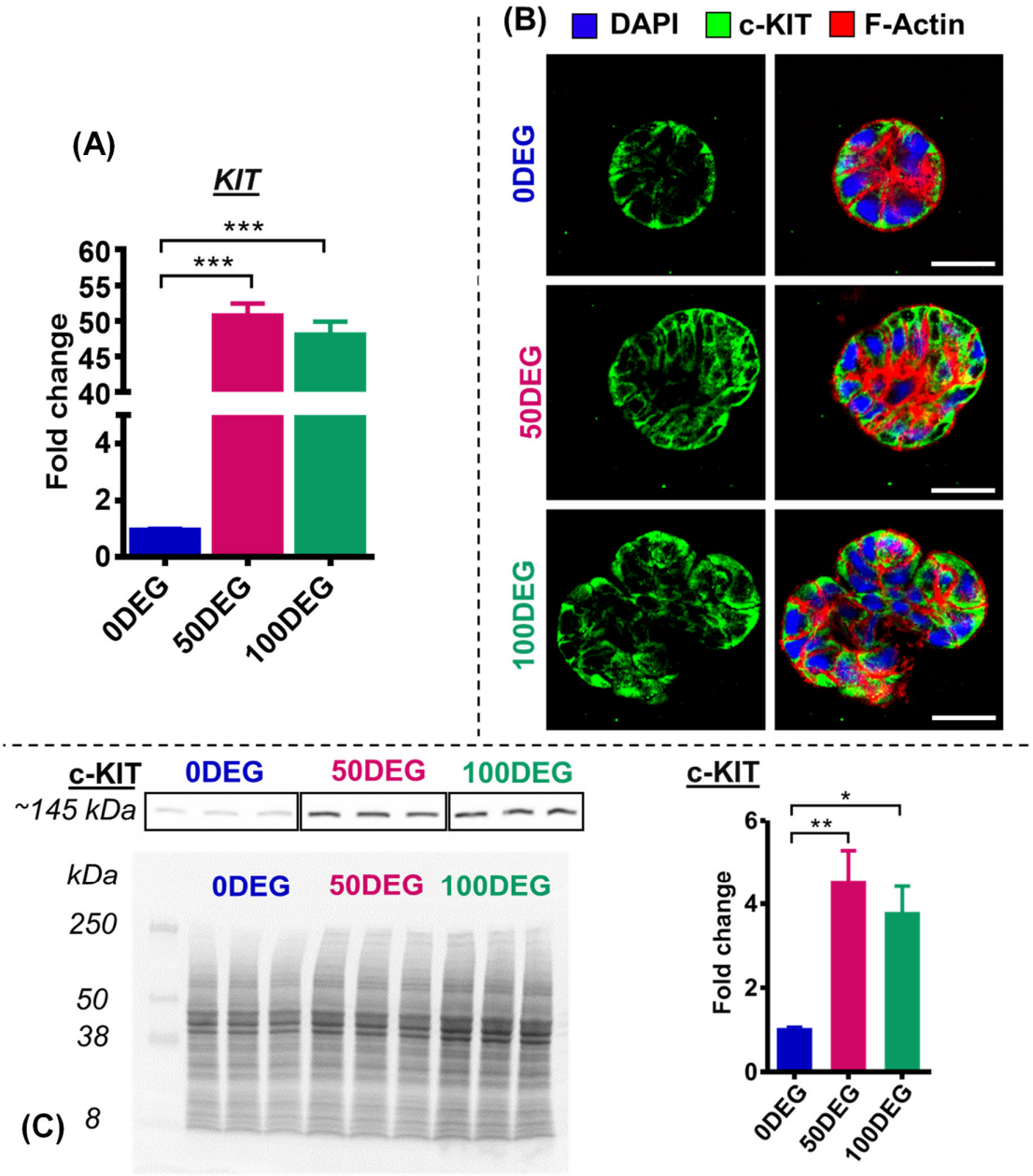

Figure 7. Characterization of KIT expression by day 15 constructs by qPCR (A), immunofluorescence (B), and western blotting (C). **(A)** qPCR analysis of the mRNA levels of *KIT. GAPDH* was used as the house keeping gene. Error bars represent SEM in all cases. One-way ANOVA, followed by Tukey's multiple comparison test. * indicates $p < 0.05$, ** indicates $p < 0.01$, *** indicates $p < 0.005$ between 0DEG, 50DEG, and 100DEG at the same time point. **(B)** Immunocytochemistry shows the presence of c-KIT+ (green) cells in 0DEG, 50DEG, and 100DEG cultures. Scale bar: 20 μm. **(C)** Western blot analyses of 3D cultures for

the expression of KIT. Quantitative analysis was performed by densitometry and the bar graph represents the data from the three biological replicates. Error bars represent SEM in all cases. One-way ANOVA, followed by post hoc Tukey's test. * indicates $p < 0.05$, ** indicates $p < 0.01$.

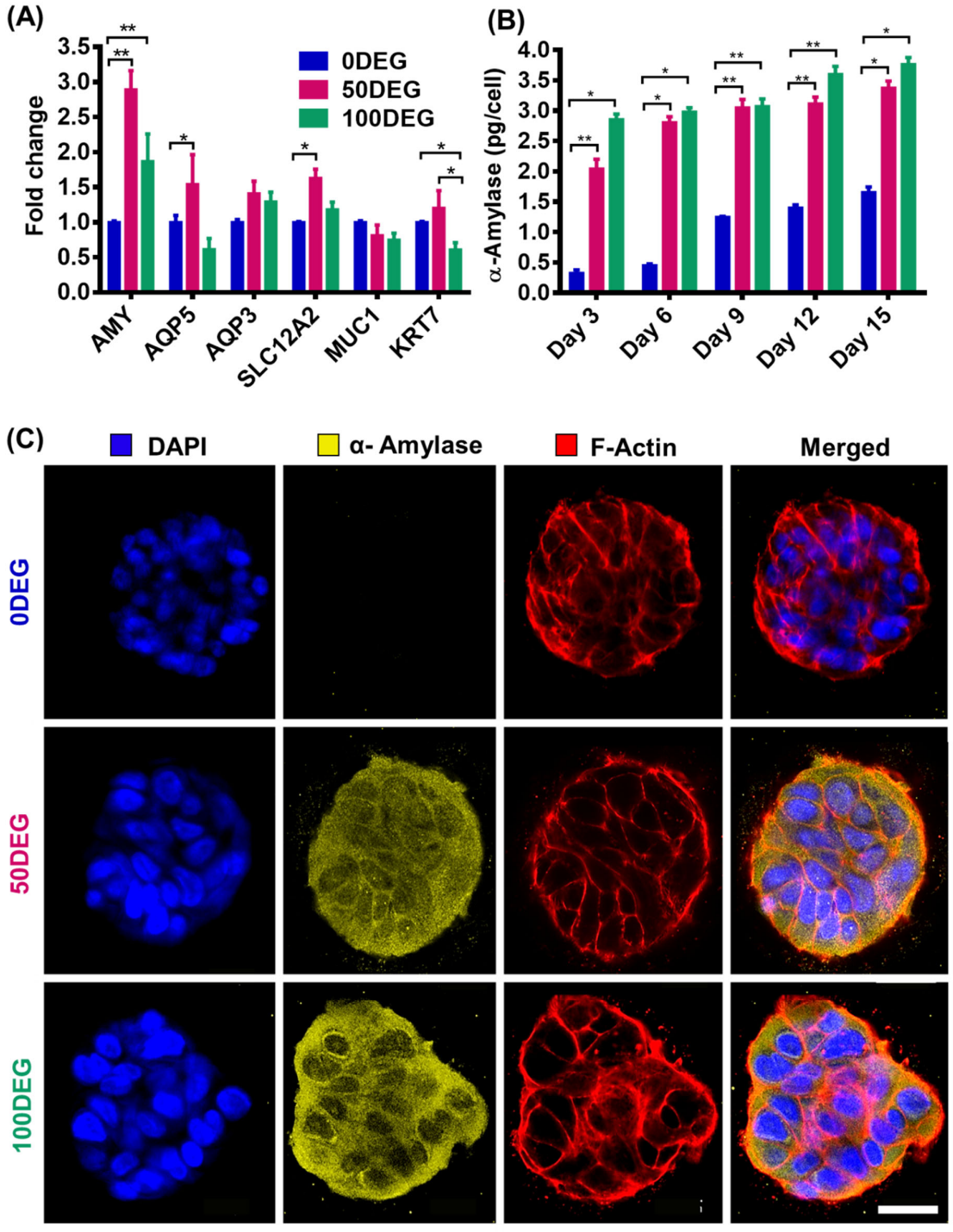

Figure 8. Characterization of the expression of differentiated markers by qPCR (A), ELISA (B), and immunofluorescence (C). **(A)** qPCR analysis of the mRNA levels of acinar (*AMY, AQP5, AQP3, SLC12A2*) and ductal (*MUC1, KRT7*) markers. *GAPDH* was used as the house keeping gene. **(B)** Quantification of α-amylase secretion in the media at days 3, 6, 9, 12, and 15. Error bars represent SEM in all the cases. One-way ANOVA were performed on data sets for (A) and (B), followed by post hoc Tukey's test. * indicates $p < 0.05$, ** indicates $p < 0.01$. **(C)** Immunofluorescence showing the distribution of amylase (yellow) in 0DEG, 50DEG, and 100DEG cultures. Scale bar: 20 μm.